NTNU

Norwegian University of
Science and Technology

Optical Studies of Single Semiconductor Nanowires by Micro-Photoluminescence Spectroscopy

Thomas Andre Karlberg

Master of Science in Electronics
Submission date: June 2010
Supervisor: Helge Weman, IET
Co-supervisor: Fervin Moses Anthonysamy, IET
                         Jelena Todorovic, IET

Norwegian University of Science and Technology
Department of Electronics and Telecommunications

Problem Description

The purpose of this master thesis is the optical studies of single semiconductor nanowires by the use of micro-photoluminescence (µ-PL) spectroscopy at low temperature. The nanowires have been grown by Au-catalyzed MBE, and the structures to be examined are GaAs nanowires with a GaAsSb insert, both with and without AlGaAs coating. The nanowires will be subject to µ-PL spectroscopy in combination with transmission electron microscopy (TEM) in order to further study the effects of structural defects on the optical properties of the nanowires. Possible effects of TEM study on nanowire optical properties will also be examined. In order to examine further study the physics of optical recombination in the nanowires, µ-PL polarization studies of the nanowires will also be carried out.

Assignment given: 21. January 2010
Supervisor: Helge Weman, IET

Acknowledgments

There are quite a few people I would like to thank for helping me wrap my head around the different aspects of this thesis. This is mainly attributed to the fact that everyone I have talked to have displayed an extreme thirst for knowledge combined with excellent manners. Every question I have directed towards these people have always been met with enthusiasm and almost unbelievable talents to make the incomprehensive understandable. Although sitting on the cutting edge of knowledge on their respective fields, they have never been afraid to answer "*we can't really say*" or "*I don't know*", a Jedi trick I to a certain extent feel I have yet to master. It has certainly been a pleasure to work in the presence of these bright minds, and I would like to direct a few words to specific individuals for their help during the past year.

- *Fervin Moses Anthonysamy* has spent a considerable amount of hours with me, and I am simply astonished that he had the patience to stay cheerful through all of my quite frequent questioning. He has also been quite helpful in tipping me what to look into deeper for my thesis, but I would also like to say "*Thanks for keeping me from blowing up the lab!*", something I undoubtedly would have done without his help.

- *Lyubomir Ahtapodov* has also spent a lot of time with me. Although mainly not in the lab, he has been extremely helpful to me by explaining what I would call difficult theory to me. I was very impressed by the degree of expertise he could offer, and the amount of time he was willing to spend helping people like me gain much needed knowledge.

- *Jelena Todorovic* impressed me with her incredible cheerful behavior and the level of interest she showed for everything. I am especially grateful to her for helping me acquire a deeper understanding of the crystal structure of our nanowires, and the nature of the different structural defects. I would also like to thank her for letting me sit in on several of the TEM sessions, although I'm sure it was stressful enough with a stubborn CM30, even without my presence.

- *Prof. Helge Weman* is a man I can only describe as incredibly knowledgeable. If his is the level of understanding needed to become a professor, I am sure I will never become one. Although his schedule is as full as his experience, he has never given the expression of not having time to talk. I would even go as far as to say that his welcoming nature gives rise to increased enthusiasm and dedication for everyone working on the nanowire project.

Abstract

Over the recent years semiconductor nanowires have gained much attention for their potential to either improve existing technology or create novel devices. This potential has been realized in devices such as semiconductor nanowire lasers[2-3] and nanowire single-photon detectors[4]. With nanowire technology it could be possible to create single-photon nanowire lasers that emit photons in the near infrared region. Such devices should prove very interesting for telecommunications and quantum cryptography.

The purpose of this master thesis was the study of the optical properties of GaAs nanowires with GaAsSb inserts. For this reason, both nanowires with and without an AlGaAs coating to increase the nanowire Quantum Efficiency (QE) have been subjected to low temperature PL spectroscopy. In an attempt to determine the physical origin of the different optical properties of different nanowires, μ-PL spectroscopy, Scanning Transmission Electron Microscopy (STEM) and Transmission Electron Microscopy (TEM) was carried out on the same nanowires of a sample with AlGaAs shell nanowires. Through these measurements, it was found that STEM at 30 kV did not change the optical properties of the nanowire, but 200 kV TEM had a detrimental effect on nanowire PL. Through the structurally and optically correlated examination, it was found that stacking faults near the insert was not the origin of the power dependent behavior of the insert emission, and in combination with PL measurements of both zincblende (ZB) and wurtzite (WZ) GaAs nanowires the electronic band structure of the nanowire inserts was determined to very likely be type-II. Also, a theoretical explanation of the origin of the observed insert emission behavior was presented, and polarization dependent PL measurements were presented and discussed.

Table of Contents

List of figures

List of tables

Nomenclature

PL	Photoluminescence
CMOS	Complementary metal-oxide-semiconductor
QD	Quantum Dot
CVD	Chemical Vapor Deposition
MBE	Molecular Beam Epitaxy
ZB	Zinblende (cubic crystal structure)
WZ	Wurtzite (hexagonal crystal structure)
E_g	Band Gap Energy
UPB	Upper Polariton Branch
LPB	Lower Polariton Branch
DH	Double-Heterostructure
CCD	Charge-Coupled Device
BS	Beam Splitter
FWHM	Full Width at Half Maximum
NW	Nanowire
STEM	Scanning Transmission Electron Microscopy
TEM	Transmission Electron Microscopy

1. Introduction

Downsizing of electronic circuits with traditional lithography techniques becomes increasingly more expensive as problems are encountered by approaching fundamental physical limitations of small size devices[5]. It is evident that at some point a new generation of components must replace or contribute to the well established CMOS technology in order to improve device functionalities. For this reason, the interest for semiconductor nanowires has grown significantly over the recent years. Nanowire technology show great potential to create miniaturized and more effective components within various fields of technology. After two decades of research, different nanowire devices have been demonstrated. Semiconductor nanowire lasers[2-4] , nanowire single-photon detectors[4] and nanowire waveguides[6] have shown us that nanowires have the potential to become the building blocks of future generation electro-optical devices. Other nanowire-based technologies such as chemical and gas sensors[7] and nanowire field-effect transistors and biosensors[8] have also been developed.

Because of the small size of nanowires, reduced dimensionality can make effects from quantum mechanics prominent in the physical properties of the nanowire. By taking advantage of these effects, new and interesting devices that would be difficult, if not impossible, to manufacture with standard lithography can take shape. Controlling composition along the nanowire makes it possible to create quantum dots (QDs) in nanowires. In QDs the energy states become quantized, and nanowire single-photon sources can be produced[9]. This type of single-photon source combined with nanowire photonic crystals[10] should prove very interesting for fiber telecommunications and quantum cryptography.

Nanowires are usually synthesized by the vapor-liquid-solid (VLS) method, where a metal catalyst is used to grow standing nanowires on a substrate by either chemical vapor deposition (CVD) or molecular beam epitaxy (MBE). The nanowires to be examined in this thesis are grown by MBE in the <111> direction. Until recently, the GaAs nanowires grown by MBE have shown a WZ crystal structure, unlike bulk GaAs which is ZB. However, through controlling growth parameters, GaAs nanowires with ZB crystal structure grown by MBE has been proven possible[11-12] .

In this thesis, GaAs nanowires grown by MBE will be subjected to micro-photoluminescence (μ-PL) at low temperatures (4-20 K) in order to study their optical properties. The GaAs nanowires have a core diameter of 40 to 50 nm, and are typically 2 to 3 μm long. They also have inserts of GaAsSb about 30-50 nm long for band gap engineering. The crystal structure of the insert is ZB while the GaAs is WZ. However, also nanowires of ZB GaAsSb and ZB GaAs will be examined in this thesis. In order to improve the quantum efficiency of the nanowire, some of the wires have an AlGaAs shell approximately 20 nm thick, and a GaAs cap approximately 2 nm thick to prevent AlGaAs oxidation.

The WZ and ZB crystal structures of the nanowires both suffer from occurrences of structural defects to be explained in more detail in the Theory section. These defects complicate the electronic band structure of the nanowire, and thereby also the interpretation of the PL-measurements. In an attempt to correlate specific optical behavior with a certain nanowire structure, nanowire samples will be subject to both low temperature PL spectroscopy and TEM. In further attempts to gain more detailed information about the origin of specific emission lines in the PL-spectrum, polarization dependence will be done in combination with power dependent μ-PL measurements for certain nanowires.

2. Theory

2.1 Energy bands in bulk materials

It is a well known fact that the electron energy states in a free, single atom are discrete, as only certain well defined energy states are allowed for a specific number of electrons. These energy levels are defined by the lowest possible potential energy of an electron, considering the attractive and repulsive forces between the atom core and electrons. The allowed energy states of the electrons are separated by energy intervals consisting of illegal electron energy states. The number of electrons allowed per energy level is described by the Pauli exclusion principle, stating that electrons with the same quantum state can not occupy the same area in space (and therefore same energy levels). This means that only two electrons, spin up and spin down, can occupy the inner shell. While additional middle and outer shells may support a greater number of electrons as the number of electron quantum states increase, the number of electrons allowed in each shell is still limited, as seen on the right side of Figure 2.1.1.
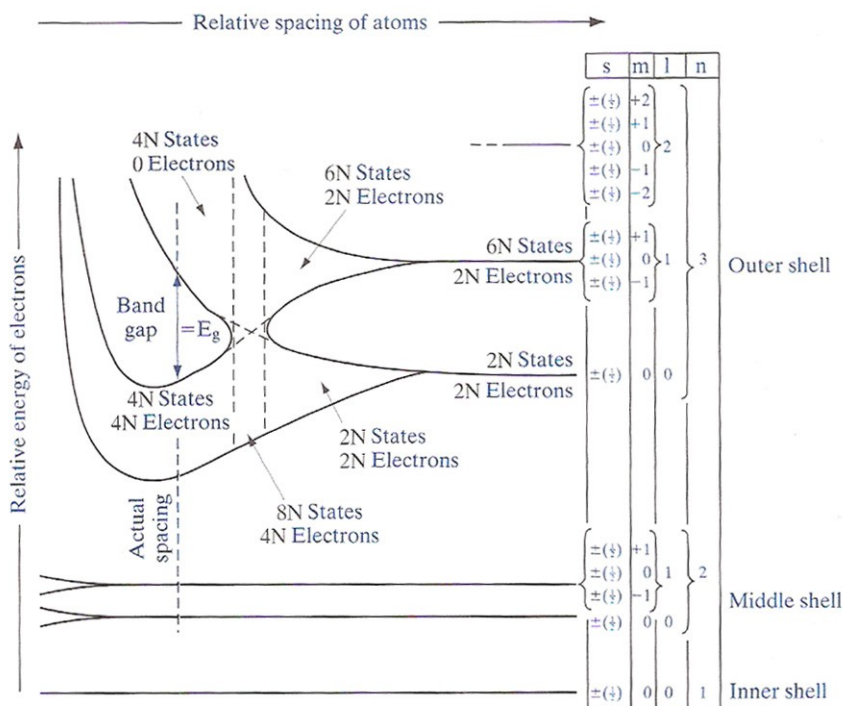
Figure 2.1.1. Electron energy levels of Si as a function of interatomic spacing[13].

Figure 2.1.1 shows the change in energy levels as free atoms bond to form a solid. When the atoms bond, the discrete energy levels are clearly affected. This is because the wave function of the outer shell electrons in the neighboring atoms start to overlap, as the valence electrons of one atom feels the influence of another atom. As the atoms bond, the discrete electron energy levels change into

3

energy bands of allowed energy states with band gaps of illegal energy states separating them. This band structure is specific for different solids, and can explain the difference between insulators, semiconductors and metals.

For an electron to move in the presence of an electric field, there must be unoccupied energy states nearby to which the electron can move. Electrons naturally fill up energy states from lowest to higher energy states. Considering the case where there is a band gap between a lower filled energy band and a higher empty energy band, electrons can not move in the lower, filled band as there are no vacant legal states to travel. The same can be said for an electron hole (absence of an electron) in the upper, empty band.

However, if an electron is excited from the lower band to the upper band it is free to move as there are many vacant states nearby. By moving between these vacant states, the electron can transport charge in the presence of an electric field. In the same way, an electron hole created in the valence band is also free to move. It is therefore logical to call the lower, filled band the valence band, and the upper, empty band the conduction band.
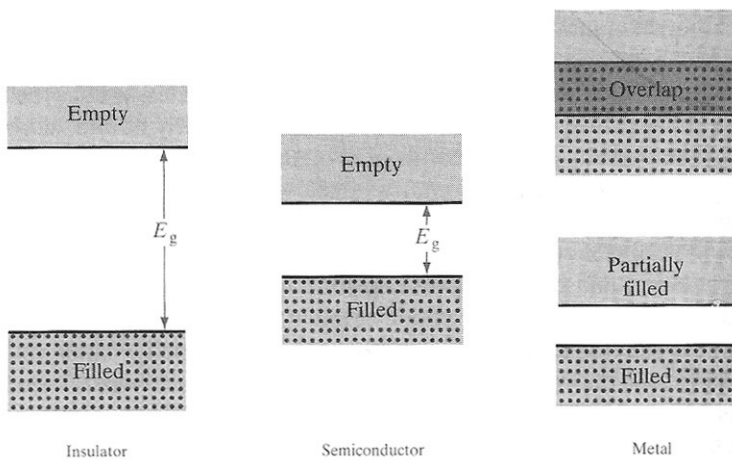
Figure 2.1.2. Typical band structure of insulators, semiconductors and metals at 0 K[13].

The fundamental difference between insulators, semiconductors and metals is shown in Figure 2.1.2. For insulators, the conduction and valence bands are separated by a significant band gap energy (E_g), typically over 10 eV. It is therefore very unlikely for an electron to be excited from the valence band to the conduction band, and no current will flow as there are negligible amounts of electrons in the conduction band and electron holes in the valence band free to move and transport charge in the presence of an arbitrary electric field. For semiconductors, the band gap energy is

smaller, typically less than 4 eV. Excitation of electrons from the valence to the conduction band is thereby possible with reasonable amounts of thermal and optical energy, and a specific amount of free carriers (electrons in the conduction band and electron holes in the valence band) are present even at room temperature. For metals, the conduction and valence band either overlap or are partially filled, such that there are always free carriers present. This is why metals typically present very low electrical resistance.

2.2 Semiconductor band gap energy
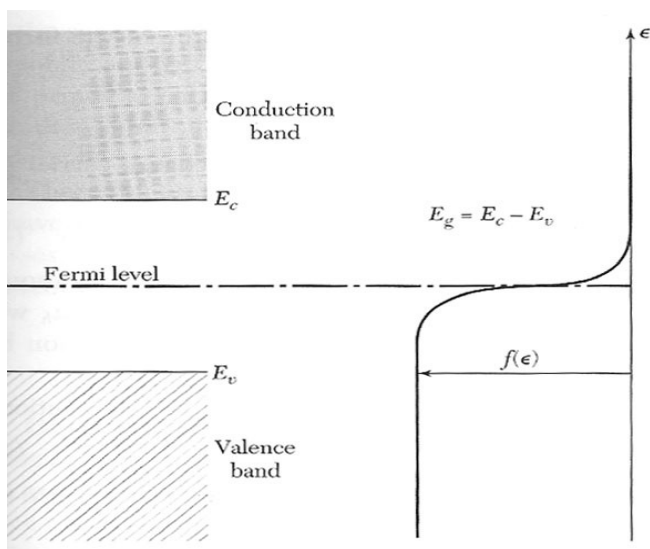
Figure 2.2.1. A general sketch of a semiconductor energy band and the Fermi distribution function[1].

Figure 2.2.1 shows the typical energy structure of a semiconductor with a valence and conduction band separated by a band gap energy of illegal states with the Fermi level close to the center of the band gap. The Fermi distribution function describes the probability of an electron occupying a specific energy state as a function of energy and temperature (disregarding the state being allowed or illegal). The Fermi level is the energy level at which the probability of occupancy is 0.5. As described in section 2.1, the value of the band gap is specific for different types of semiconductors. The band gap energy of the different semiconductors involved in this project is presented in Table 2.2.1. The electronic band structure of semiconductors also depend on temperature, crystal structure and strain.

At 0 K, the Fermi distribution has the form of a step function. This implies that the valence band is filled with electrons, and the conduction band is empty. As the temperature increases, the Fermi distribution smooths like in Figure 2.2.1, and there is an increase in the probability of electrons

being excited from the valence band to the conduction band.
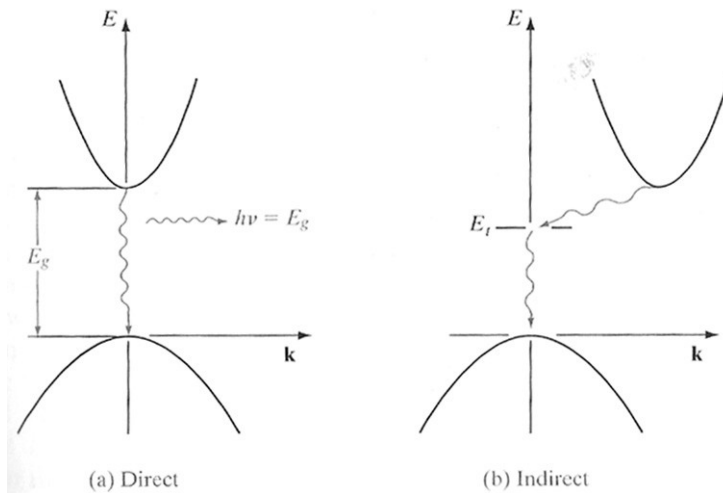
Figure 2.2.2. Direct (a) and indirect (b) transition in an arbitrary semiconductor[13].

As shown in Figure 2.2.2, semiconductor band gaps are classified as either direct band gap or indirect band gap. Electronic band structure can be described as a function of the electrons wave vector (k). In direct band gap semiconductors, the lowest point of the conduction band and the highest point of the valence band is at the same k-value. For indirect band gap semiconductors, the minimum of the conduction band and the maximum of the valence band is not at the same k-value. For an indirect transition, the electron must change its momentum by phonon interaction. For optical devices, direct band gap semiconductors are almost always used, as indirect recombination is far less effective concerning light emission. The semiconductor compounds used in this project are direct band gap.

A semiconductor can be doped with donors and acceptors. Donors and acceptors are impurities introduced to the crystal structure of the semiconductor that produces bound electron states slightly below the conduction band and bound electron hole states slightly above the valence band respectively, thereby respectively increasing or decreasing the Fermi level.

Material	E_g (T = 300 K)
GaAs(ZB)[14]	1.42 eV
$Al_xGa_{1-x}As$[15]	$(1.42+1.36x+0.22x^2)$ eV (x<0.4), $(1.91+0.21x+0.06x^2)$ eV (x>0.4)
$GaAs_{1-x}Sb_x$[16]	$(1.42-1.9x+1.2x^2)$ eV (x<0.3)

Table 2.2.1. Band gap energies of different semiconductors relevant for the project work.

It is possible to optically excite electrons from the valence band to the conduction band by pumping the semiconductor sample with a laser emitting at a wavelength corresponding to a higher energy than the band gap energy of the semiconductor[1]. In order to study the photoluminescence of the semiconductor samples shown in Table 2.2.1, it is sufficient to use a laser with a wavelength shorter than 568 nm to optically excite the samples. The relation between photon wavelength and photon energy is given by (1).

$$E = h\nu = h\frac{c}{\lambda} \Leftrightarrow E[eV] = \frac{1239.842 eVnm}{\lambda[nm]} \tag{1}$$

2.3 Exciton

A free electron hole in the valence band and a free electron in the conduction band can become bound through Coulomb interaction to form a quasi-particle known as an exciton. A free exciton is free to move in the solid, but unlike a free electron or electron hole, the exciton can not transport charge since the exciton has no net charge.

As will be shown in section 2.4, the recombination of a free electron at the bottom of the conduction band and a free electron at the top of the valence band will result in the emission of a photon with an energy equal to the band gap energy. For an exciton, the total energy of the particle is lowered in relation to the band gap, since the potential energy of the electron is lowered by binding to the electron hole and vice versa. The amount of energy involved in the formation of a free exciton is called the exciton binging energy. The recombination of a free exciton would therefore result in an emitted photon with energy equal to the energy band gap with the exciton binging energy subtracted. Since the exciton binding energy is 4.2 meV in GaAs[1], the energy of a photon emitted from a free exciton annihilation would be 4.2 meV lower than the energy band gap.

Excitons can also become bound to a neutral or ionized impurity, and in that manner reduce the energy of the quasi-particle even further. The emission lines from these bound excitons in a PL spectrum will be characteristic for each type of impurity, and can provide useful information about semiconductor quality.

2.4 Radiative recombination mechanisms in semiconductors
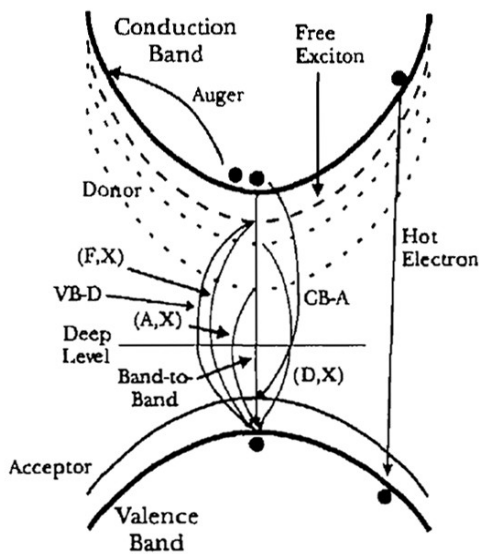
Figure 2.4.1. Different types of recombination mechanisms[17].

Figure 2.4.1 shows different recombination mechanisms responsible for radiation at different energy levels in a direct band gap semiconductor:

1. Recombination of a free electron and a free hole (band to band recombination)
2. Recombination of hot carriers (free electrons and holes that have not relaxed to the lowest energy state of the conduction and valence band)
3. Recombination of a free exciton (F, X) (See section 2.3)
4. Donor-to-valence band recombination (VB-D) (electron bound to donor recombines with a free hole)
5. Conduction band-to-acceptor (CB-A) (a free electron recombines with a hole bound to an acceptor)
6. Donor-acceptor pair emission (an electron bound to donor recombines with a hole bound to an acceptor, highly sensitive to the distance between the acceptor and donor impurities)

The first type of recombination results in emission of a photon with a wavelength corresponding to the energy band gap of the semiconductor, as given by (1). The second type of recombination would result in emission of a photon with higher energy than the energy band gap, meaning a photon with shorter wavelength than the first type. The four last types of radiative recombination occurs slightly below the band gap energy, since carriers decrease their potential energy by binding to other particles, resulting in photons with slightly longer wavelength than the first type.

8

These different mechanisms may be visible as discrete peaks in the emission spectrum at very low temperatures. As temperature increase, the different peaks widen and merge into a single wide peak as carriers start to occupy higher energy states and phonon interaction becomes more likely. In a high quality GaAs/AlGaAs double heterostructure sample, the free exciton peak is distinguishable from the donor bound exciton at 10 K, but merge into one peak at 30 K[17]. This means that to observe free exciton emission in GaAs, low sample temperature is critical.

2.5 Introducing nanostructures

In the previous sections, only properties of bulk semiconductors have been presented. Bulk semiconductors are samples that have no reduced dimensionality, in other words samples that are greater in size than the de Broglie wavelength of an electron at the Fermi level in all dimensions. The dimensions of a structure can however be reduced in such a way that carriers become confined to smaller regions of space. As this happens, the density of states in the solid changes, and carriers can be restricted to move in only two, one or no spatial dimensions. These type of structures are called quantum wells, quantum wires and quantum dots respectively. In quantum wires, the dimensions in direction perpendicular to the length of the wire are so small that carriers are somewhat restricted to move only along the length of the wire.

The de Broglie wavelength in doped GaAs is approximately 50 nm[18], and greater for intrinsic GaAs. Since the diameter of the nanowires to be studied in this project are 40 - 50 nm, the one dimensional quantum confinement effect described above should dictate the behavior of carriers in these wires.

If the compositions of different semiconductor elements is controlled along the length of this wire, it is possible to introduce an insert where the composition of elements is different from the rest of the wire. If the band gap of the insert is smaller than that of the rest of the wire, carriers can become confined within the insert (see section 2.9), thereby reducing the dimensionality of the structure even further. Since this structures dimensionality is reduced in three dimensions, this quantum well inside a quantum wire corresponds to a quantum dot.
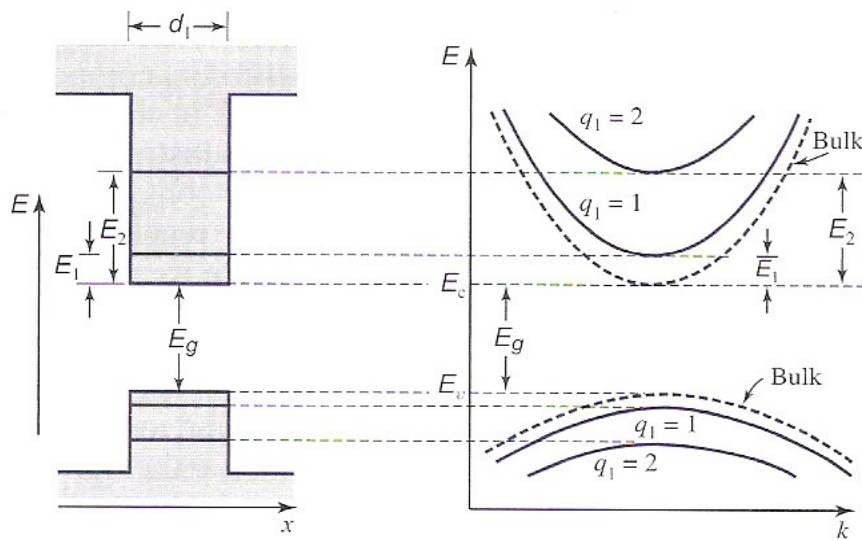
Figure 2.5.1. The effects of strong quantum confinement on energy states in semiconductor band structure[18].

Figure 2.5.1 shows the effect of strong quantum confinement of carriers on a semiconductors electronic band structure. Since the length of the inserts in the wires, which is typically $30 - 50$ nm, and the diameter of the wires are both smaller than the de Broglie wavelength in GaAs, one can expect that the density of states in the wire changes so that the energy states in the electronic band structure become quantized as shown in Figure 2.5.1. However, this is for free carriers. Since this project studies low temperature photoluminescence, free carrier recombination is not the prominent source of emission. When the thermal energy is lower than the exciton binging energy, which is true below 48 K in GaAs, electrons in the conduction band and holes in the valence band will combine to excitons, as the exciton is the lowest possible energy state and the thermal energy of the system is not high enough to break the exciton bond.

The exciton energy states are not expected to become quantized as the electronic band structure has before the dimensions of the samples approach the Bohr radius of the exciton. In GaAs, the Bohr radius of the exciton is 11.6 nm[19], which is rather small compared to the dimensions of the nanowires to be studied in this project. The exciton should not be "pressed" in any way, and exciton energy states are not expected to become quantized. Low temperature PL spectrum is therefore expected to be quite similar to bulk materials for the nanowires to be studied in this thesis before taking the crystal structure into account.

2.6 Synthesizing nanowires

Growing wires of the size as mentioned in section 2.5 can be done by the VLS mechanism developed by Wagner and Ellis in 1964[20]. This method takes advantage of the fact that direct adsorption of gas particles on to a solid generally is quite slow. By introducing a liquid stage, crystal growth speeds up and introduces new options for growth control. Figure 2.6.1 shows how the VLS method accomplishes this. Gold (Au) is deposited on a substrate as a catalyst. Various methods exists that control the size and or position of the deposited areas, since the nanowire diameter greatly depends on the diameter of the gold particles. Applying the Wagner and Ellis method originally developed for growth of silicon whiskers to III-V nanowires like GaAs is not completely straightforward[21]. After annealing, the Au is alloyed with Ga from the substrate and melts. To grow GaAs nanowires, Ga and As vapor is introduced with Molecular Beam Epitaxy (MBE) in this thesis at the correct growth temperature. If the growth temperature is above 620 ºC the alloy droplet segregates on the substrate surface making nanowire growth impossible, while 320 ºC seems to be the lower limit for nanowire growth. The growth temperature used for axial growth of GaAs nanowires in this project is 540 ºC. The vaporized particles of Ga and As are adsorbed into the Au droplet, until the droplet reaches a supersaturated level. As this happens, crystal growth starts in the <111> direction from nucleated seeds at the liquid-solid interface, as shown to the right in Figure 2.6.1.
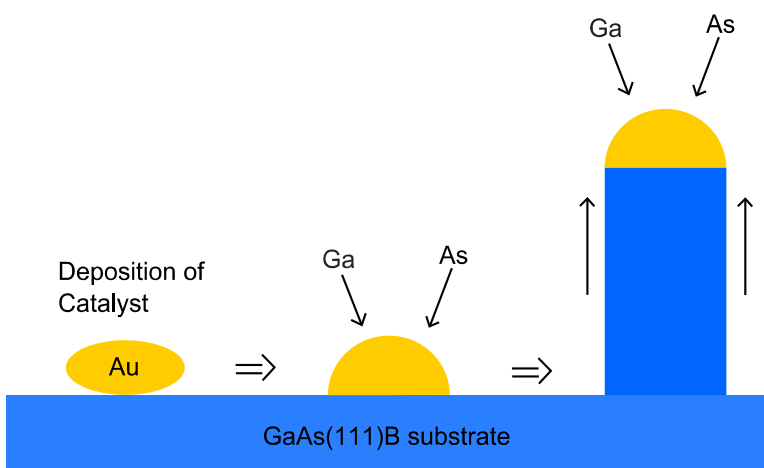
Figure 2.6.1. VLS growth of GaAs nanowire.

By controlling which atoms are introduced in the MBE, it is possible to engineer both axial and radial heterostructures in the nanowire. As only Ga and As is present in the molecular beam in the beginning of the growth, a pure GaAs semiconductor nanowire is formed. By abruptly introducing a flux of Sb, the nanowire quickly starts to grow GaAsSb. After a short growth period, growth interrupt is performed. This is done by stopping the flux of As and Sb for approximately one minute, thereby evaporating As and Sb from the alloy droplet since As and Sb are quite volatile

compared to Ga. By then introducing As again, the nanowire continues to grow GaAs. In this way, an axial heterostructure as shown in Figure 2.6.2 can be formed.
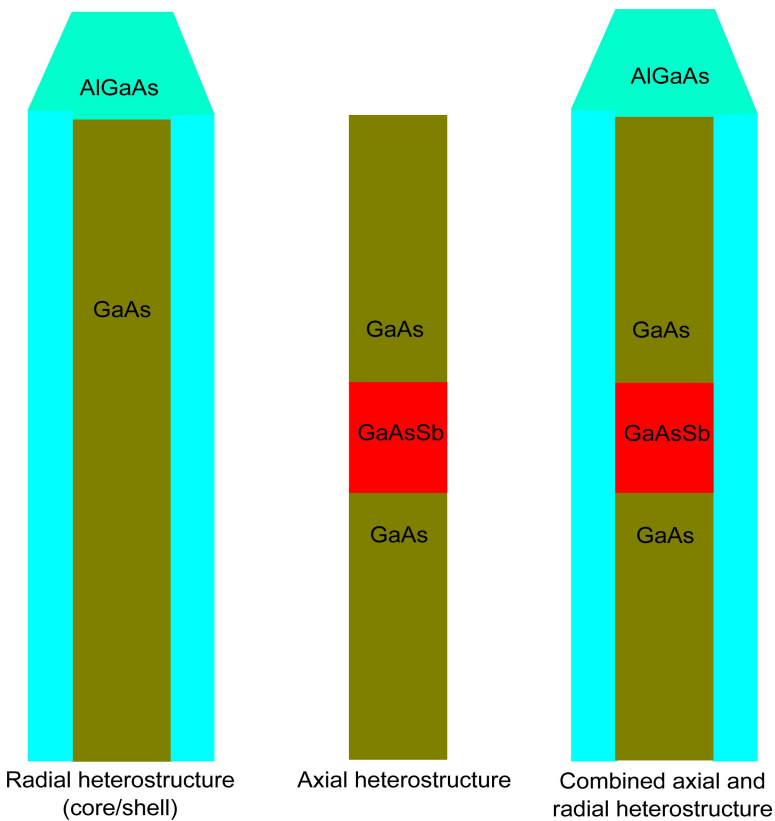
Figure 2.6.2. Nanowire radial and axial heterostructures.

Ga atoms in the vapor landing on the substrate or on the sidewall of the nanowire can diffuse up the wire to the alloy droplet, where it can contribute to the nanowire growth. The diffusion length of Ga is so long that it is possible to grow GaAs nanowires up to 3 μm long with practically only axial growth. This is not the case for Al, as the Al vapor atoms do not have as long diffusion length. If Al vapor is introduced when the nanowires are between 2 and 3 μm, the nanowire will start to grow AlGaAs both radially and axially. Therefore, the addition of Al to the vapor at the correct time during growth is enough to grow an AlGaAs shell around the nanowire core, a type of radial heterostructure as shown in Figure 2.6.2. In order to keep the AlGaAs from oxidizing, it is prudent to grow a small GaAs cap around the AlGaAs shell. Since the Ga atoms display such a long diffusion length, the growth temperature must be reduced to support a substantial radial growth.

The nanowires to be measured in this master thesis have been grown by the method described in this section. The nanowires are therefore approximately 2 − 3 μm long, and have a GaAs core approximately 50 nm in diameter, with GaAsSb inserts approximately 50 nm long. Both wires with and without an approximately 20 nm AlGaAs shell have been grown, and the AlGaAs shell wires have a GaAs cap around 2 nm thick.

2.7 Nanowire crystal structure

Normally, bulk GaAs only exists in the ZB crystal structure, the same cubic crystal structure as diamond. However, for nanoscale volumes, the hexagonal WZ structure of GaAs is stable. MBE grown GaAs nanowires with supersaturated alloy droplet preferably displays the WZ structure. Figure 2.7.1 shows the crystal structure of WZ and ZB of GaAs nanowires along the growth direction. Since the angles and distances between the different atoms are changed for the different crystal structures, the electronic band structure of GaAs is different for WZ and ZB. This will be discussed further in section 2.9 and 2.11.
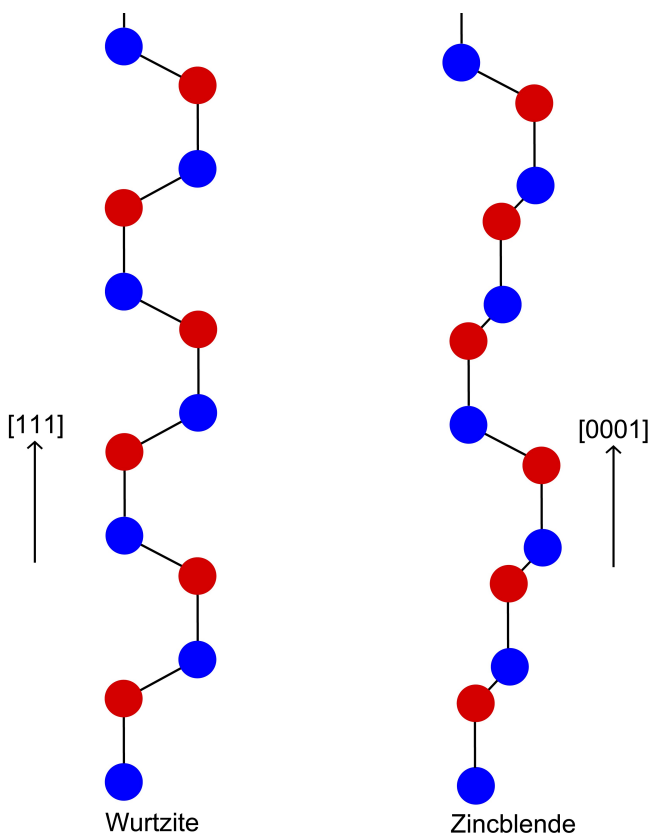
Figure 2.7.1. Wurtzite and zincblende crystal structure along nanowire growth direction.

While the WZ stacking can be mapped as ABABABAB, where each letter represents a bilayer along the [111] direction, the ZB stacking can be mapped as ABCABCABC along the [0001] direction. Both WZ and ZB nanowires can suffer from structural defects along the wire, such as stacking faults. Stacking faults are segments of a different crystal structure from the surrounding. For example, a misplacement of a single bilayer in WZ can be described as a stacking of ABAB<u>C</u>BCBC[11]. Since this corresponds to a segment of ZB surrounded by WZ, this is called a stacking fault in a WZ structure. For ZB, a misplacement of a single bilayer is not enough to create a segment of WZ. This misplacement corresponds to a 60º rotation of the crystal structure around

the axis of the nanowire, and can be described as a stacking of ABCAB<u>C</u>BACBA. Because there is no segment of WZ, this is not a stacking fault, but rather a twin since the crystal structure is mirrored in the twin plane denoted by the underlined letter. In other words, two consecutive twin defects are necessary to produce a stacking fault of WZ in ZB.

The nanowires to be studied in this thesis mainly consist of WZ structured GaAs core with a ZB structured GaAsSb insert. The crystal structure of an AlGaAs shell copies the core in such a manner that there is WZ structured AlGaAs coating around WZ GaAs, and ZB structured AlGaAs coating surrounding the ZB GaAsSb insert. However, structural defects as described earlier in this section may complicate this picture. While twin defects in the ZB GaAsSb insert are not that common as a single nanowire often has no twins or a single twin, short stacking faults of ZB GaAs of variable length in WZ GaAs may quite frequently occur. Stacking faults in WZ GaAs nanowires and the subsequent change in the electronic band structure is discussed further in section 2.11.

2.8 Passivation layer
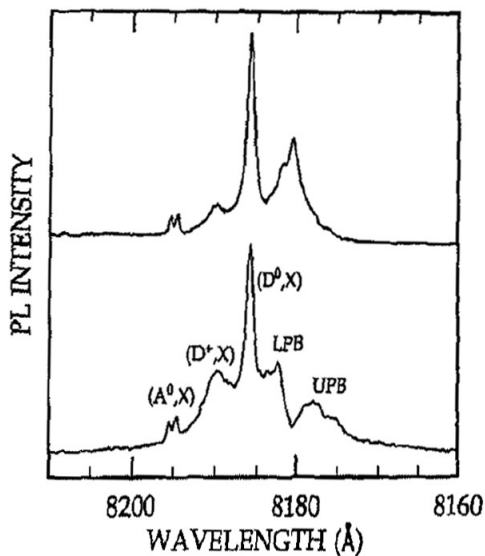
Figure 2.8.1. PL spectrum of a GaAs/AlGaAs double heterostructure
with top AlGaAs layer (top) and without top AlGaAs layer (bottom)[17].

Figure 2.8.1 shows the PL spectra of a high-quality GaAs/AlGaAs double heterostructure with and without a passivation layer. Imperfections in semiconductor surface and interfaces can induce surface and interface states, which severely affects free exciton recombination. As nanowires have a very large surface-to-volume ratio compared to bulk materials, surface states can be severely destructive for free exciton emission. In Figure 2.8.1, the free exciton emission peak is clearly visible in the spectrum with an AlGaAs passivation layer. After etch removal of the passivation layer, the free exciton emission peak splits into an upper polariton branch (UPB) and a lower

polariton branch (LPB). This UPB and LPB peaks are often visible instead of the free exciton emission peak in pure GaAs samples, but have been known to disappear if the sample is treated with a surface passivation layer. It has previously been observed that an AlGaAs shell acts as a passivation layer for a GaAs nanowire core[22], thereby increasing the QE of the nanowire core. As free exciton emission is important to the photoluminescence study of nanowires in this thesis, most of the nanowires to be studied have an AlGaAs shell.

2.9 Band gap structuring

As mentioned in section 2.5, it is possible to control the electronic band structure of a semiconductor nanowire along the length by controlling the composition of different elements while growing. In this way, it is possible to engineer the properties of the nanowire so that for example light is mainly emitted at a certain wavelength from a well defined spatial region. In Figure 2.5.1, such a structure is shown. As the conduction band of the insert is lower than the surrounding conduction bands and the valence band is higher than the surrounding valence bands, this structure is a type-I double-heterostructure (DH). In a type-I DH, the electrons and electron holes are confined to the same spatial region.
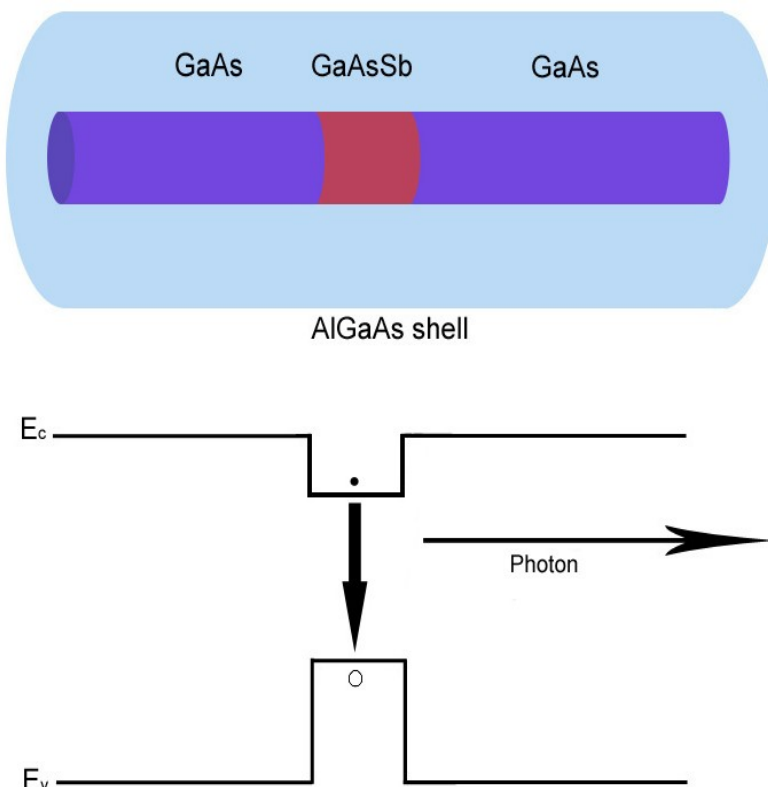
Figure 2.9.1. Expected electronic band structure of a WZ GaAs nanowire with ZB GaAsSb insert.

Figure 2.9.1 shows the expected electronic band structure of a WZ crystal structure GaAs nanowire

with a ZB structured GaAsSb insert, which is the structure of most nanowires to be studied in this thesis. Weak type-II have previously been reported from coherently strained bulk GaAs/GaAsSb multiple quantum well (MQW) structures[23], since the conduction band of ZB GaAsSb is slightly higher than that of ZB GaAs while the valence band is significantly higher. Because the crystal structure of the GaAs surrounding the ZB GaAsSb insert is WZ, as mentioned in section 2.7, and the conduction band and valence band energies of WZ GaAs is estimated to be 117 meV and 84 meV higher than that of ZB GaAs[24], the nanowires to be studied in this thesis should a type-I structure as shown in Figure 2.9.1.

If the structure were to be a weak type-II structure, the emission peak at very low excitation intensities would be lower than the energy band gap of the insert, as electrons from the lower conduction band outside of the insert would spatially recombine with holes on the other side of the junction. As excitation intensity increases, the electric field induced between electrons gathering outside the insert and electron holes gathering in the insert will lead to band bending. Also, electrons and electron holes may start to fill higher energy levels if lower energy bands start to fill up. Eventual band filling effect combined with band bending will lead to PL emission at higher energies. Since the photon energies are higher, the detected wavelength peaks move to shorter wavelengths, hence a "blue shift" of the measured power dependence spectrum.

2.10 Polarization of photoluminescence

Because of the size features of semiconductor nanowires, the polarization of nanowire photoluminescence are quite different from that of bulk semiconductors. The diameter of the nanowire is much smaller than the wavelength of visible light and infrared, while the nanowire length is greater. Since the dielectric constant of the semiconductor nanowire is much greater than the surrounding, this causes image effects so that emission from the nanowire is mostly polarized parallel to the nanowire axis. In this thesis, polarization of emission from a nanowire will be quantified by P given in (2), where $I_{\parallel}$ and $I_{\perp}$ is the intensity of emission polarized parallel and perpendicular to the nanowire respectively.

$$P = \frac{I_{\parallel} - I_{\perp}}{I_{\parallel} + I_{\perp}} \cdot 100\%$$

(2)

For the ZB crystal structure, the lowest energy recombination from the conduction band to the valence band is described as Γ_6 to Γ_8, which does not result in any polarization. Polarization of nanowire emission is therefore only determined by image effect, which has been calculated to be as

given by (3)[25].

$$\frac{I_\parallel}{I_\perp} = \frac{(\varepsilon + \varepsilon_0)^2 + 2\varepsilon_0^2}{6\varepsilon_0^2} \tag{3}$$

Assuming the dielectric constant of the AlGaAs shell to be approximately 10 from [26] and [27], and the surrounding environment to be vacuum, this gives P ≈ 91% (meaning a 20.5 times greater emission polarized parallel then perpendicular).

For the WZ crystal structure, the lowest energy recombination from the conduction band to the valence band is described as Γ_6 to Γ_9. From selection rules, this recombination results in photons with polarization 100% perpendicular to the nanowire axis. The total polarization effect from the nanowire will therefore be a superposition of selection rules and image effects. Taking this into account, the photoluminescence from WZ nanowires is expected to be slightly perpendicularly polarized (P ≈ -40%). Figure 2.10.1 shows the photoluminescence intensity expected from WZ and ZB GaAs/AlGaAs core/shell nanowires as a function of polarized angle from the nanowire axis.
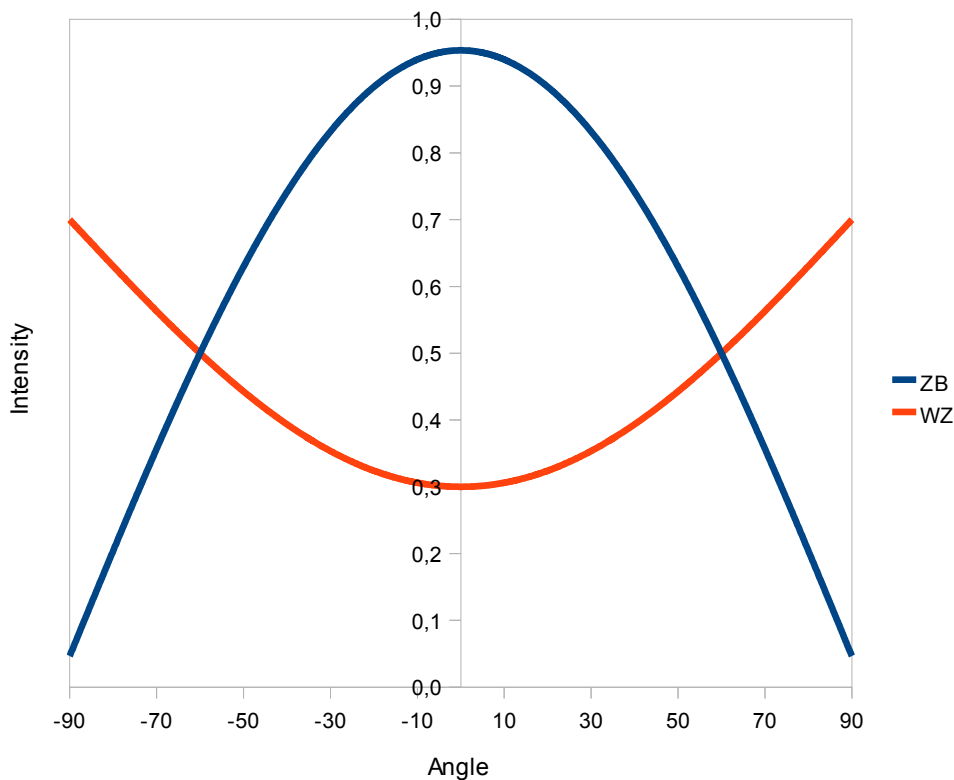
Figure 2.10.1. Expected relative PL intensity of WZ and ZB GaAs/AlGaAs nanowires as a function of angle from nanowire axis.

2.11 Stacking faults

MBE grown GaAs nanowires of WZ crystal structure may suffer from unintentional stacking faults of ZB GaAs. These stacking faults may alter the electronic band structure along the wire by introducing hetero junctions. The stacking faults are usually short enough to be represented as quantum wells for electrons as shown in Figure 2.11.1. The quantized energy states in these wells depend on the length of the stacking fault, and if the wave function of electrons confined in a well overlap with the wave function of electrons in other states than the WZ conduction band. The energy levels presented in Figure 2.11.1 are calculated by solving the finite potential well problems for electrons in GaAs, assuming that the effective masses of electrons in WZ and ZB GaAs are equal and that the stacking faults are separated by an infinite distance.
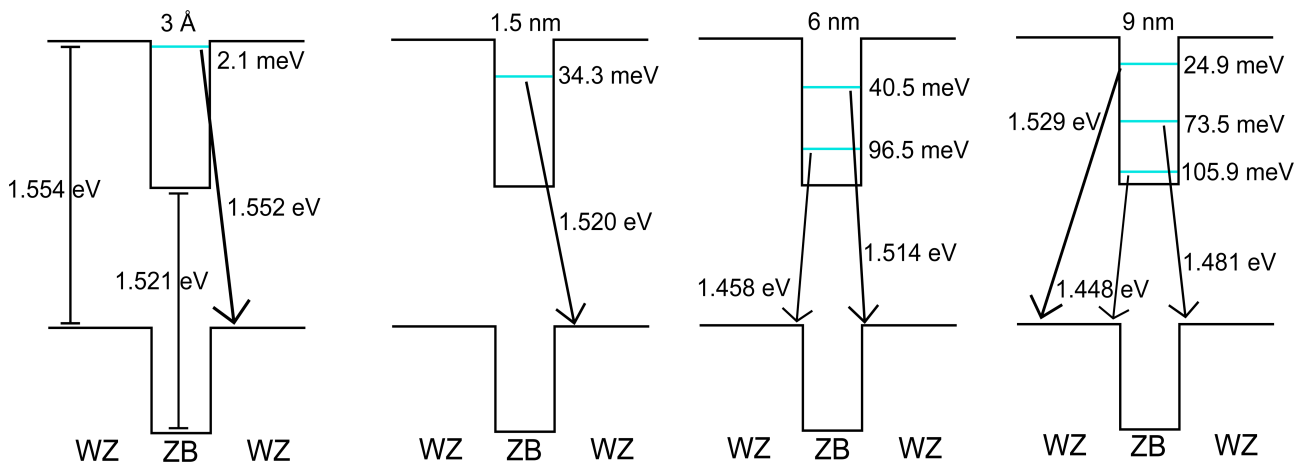
Figure 2.11.1. Quantized energy levels in ZB stacking fault induced quantum wells in WZ GaAs.

As shown in Figure 2.11.1, stacking faults of ZB in WZ GaAs can introduce PL emission peaks at lower energies than the band gap of either WZ or ZB GaAs as the hetero junctions form a type-II DH, and spatially indirect recombination of electrons in ZB recombine with holes in WZ. As mentioned in section 2.9, this type of PL peaks are expected to blue shift with band bending or "drown" in higher energy recombination with increasing excitation intensity.

In addition to unintentional stacking faults of ZB along the length of the nanowire, there may be a segment of ZB GaAs directly after the insert of ZB GaAsSb because of growth interrupt mentioned in section 2.6. Growth interrupt was introduced in the top interface of the insert while growing to reduce stacking fault occurrences and achieve a higher gradient in composition change[28-29] . It is believed that if GaAs nanowire growth starts before the alloy droplet is properly supersaturated, growth may be favoured in ZB crystal structure. The growth would in this case switch back to WZ when the droplet becomes supersaturated. This would lead to the electronic band structure shown in

Figure 2.11.2. Direct recombination in the GaAsSb insert would be difficult to observe until high laser excitation is applied since electrons will be confined only in the ZB GaAs part at the insert interface at low excitation intensity.
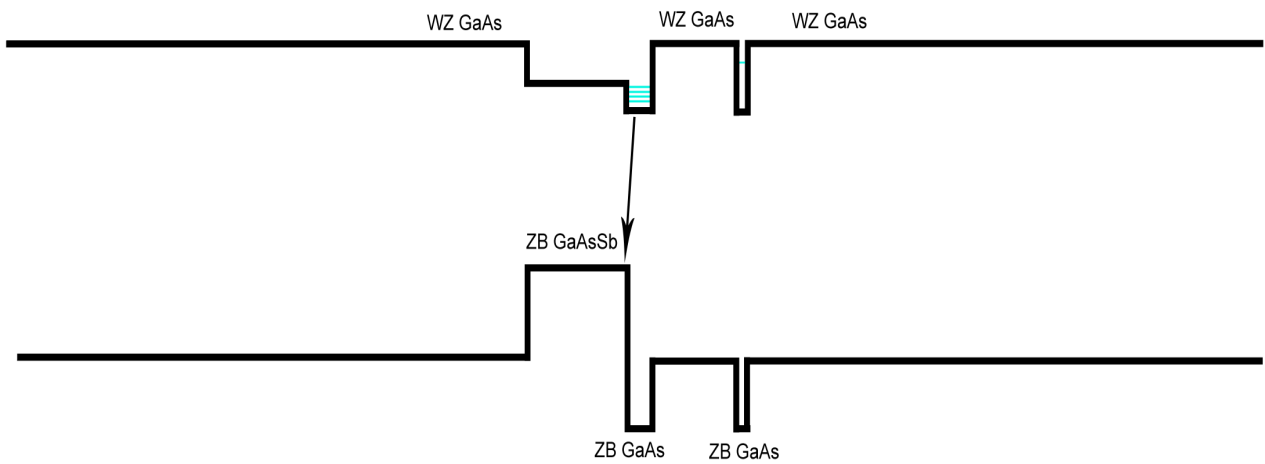
Figure 2.11.2. Unwanted recombination from ZB GaAs segment at insert.

2.12 Lattice matching
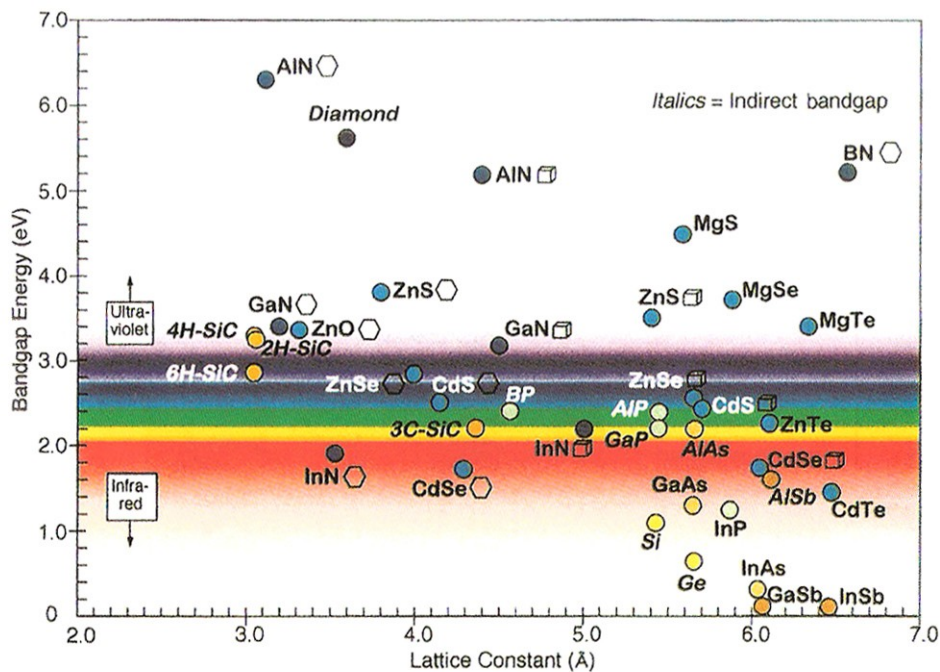
Figure 2.12.1. Lattice constant and band gap energy for different semiconductor materials[30].

Figure 2.12.1 shows lattice constants and band gap energy for different semiconductor compounds. Lattice constants are important to bear in mind, as a mismatch in lattice constants of core, shell and insert may induce strain and surface states. As seen in section 2.8, surface states can have a very deleterious effect on free exciton emission. The free exciton energies are also extremely sensitive to

strain[17]. Therefore, lattice matching is also important to consider when designing electronic band structures in addition to the band gap energies of different semiconductors. As seen in Figure 2.12.1, the lattice constants of AlAs and GaAs are very similar, but the GaSb lattice constant is roughly 8 % greater. The GaSb insert may become compressed, and the electronic band structure may be altered from the unstrained electronic band structure.

3. Equipments and Methods

3.1 Equipments

3.1.1 Laser

The laser used for optical excitation of the nanowire samples in this project was a Spectra-Physics Millennia Pro water cooled diode-pumped solid state (DPSS) laser. The laser produces a beam of up to 6 W vertically polarized continuous wave (CW) power at a wavelength of 532 nm[31]. The wavelength of the laser corresponds to a photon energy of 2.33 eV, which is more than the band gap energies of the different semiconductor compounds of the wires (see Table 2.2.1). As the laser beam from the Millennia Pro is very stable and has very low noise, the Millennia Pro is a good choice for a scientific experimental setup demanding optical excitation.

3.1.2 Spectrometer

Spectroscopy was performed with the Horiba Jobin Yvon iHR500 spectrometer. It utilizes a reflection diffraction grating to spatially distribute the photons by photon wavelength. Three different grating sizes were available (1200, 950 and 300 g/mm) for different spectral resolutions and ranges. The spectrum was routed to a CCD (Charge-Coupled Device) detector, as shown in Figure 3.1.2.1, which measured the intensity as a function of wavelength for the desired range. The spectrometer was controlled by a computer with a LabVIEW interface.
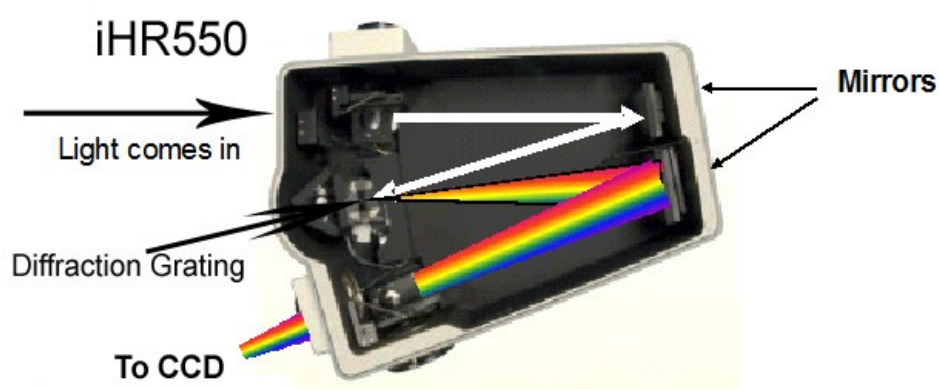
Figure 3.1.2.1. The iHR550 spectrometer.

3.1.3 CCD Detector

The CCD detector is an Andor Newton[EM] EMCCD (Electron Multiplying Charge-Coupled Device) which is optimized for high performance spectroscopic applications. The detector features low noise electronics, fast readout, cooling down to -100° C and a QE up to 95 %[32]. Because of the features of the detector, single photon sensitivity is obtained in the detector. The detector has a 1600 x 200 pixel array, and is controlled by the same LabVIEW interface as for the spectrometer.

3.1.4 Cryostat

The cryostat used in this project was a Janis ST-500 shown in Figure 3.1.4.1. This is a continuous helium flow cryostat specifically designed for microscopy imaging and high spatial resolution photoluminescence. The cryostat supports a very short working distance which permits mounting of high magnification optics. Vibration isolation and low thermal expansion of the support structure creates a very stable sample workspace with nanometer size vibration and drift levels[33]. With vacuum pumping and liquid helium flow, this cryostat is able to cool the sample down to 4 K. Very accurate manipulation of sample position is made possible in all three spatial directions by three piezos and a piezo step controller (ANC 150) from attocube.
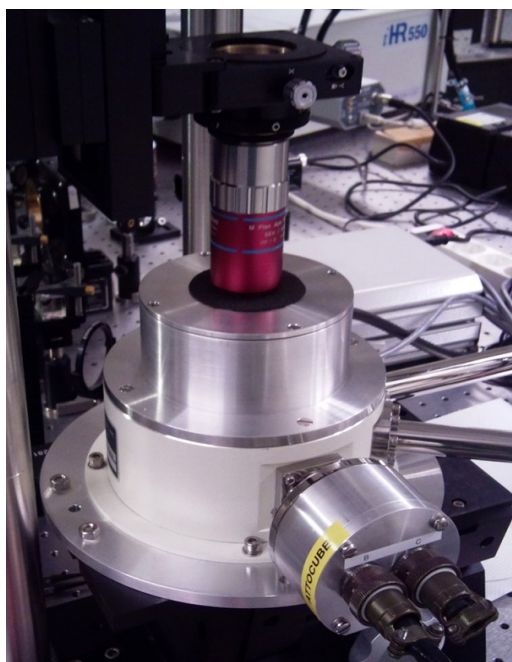
Figure 3.1.4.1. The Janis ST-500 cryostat.

3.2 Methods

After MBE-growth, the nanowires were standing wires on a substrate. To cleave off the wires, the substrate was covered with a small amount of methanol and introduced to an ultrasonic bath. The ultrasonic pressure waves broke the wires off near the bottom, and a methanol solution of floating nanowires was formed. This solution was then transferred and dispersed onto a clean sample substrate. As the methanol evaporated, the nanowires were lying along the surface of the sample substrate.

The samples were transferred and mounted to the sample holder in the cryostat. The cryostat was then vacuum pumped. When the desired pressure level of $5 \cdot 10^{-5}$ mbar in the cryostat was reached, a flow of liquid helium was utilized to cool the sample to 4-20 K. Measurements could begin as a desired and stable temperature level was reached.
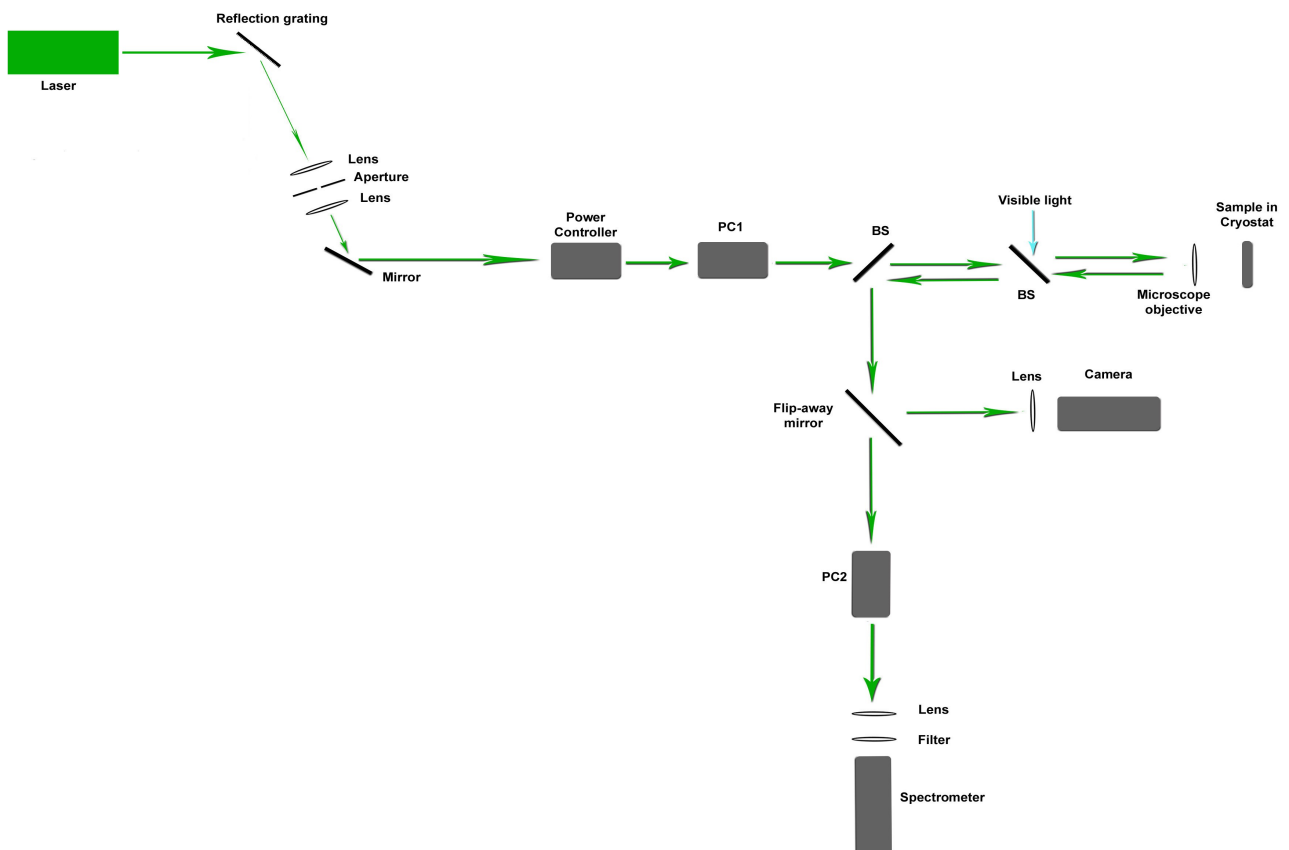
Figure 3.2.1. Optical setup for PL measurements.

Figure 3.2.1 shows the optical setup used for PL measurements. The laser was maintained at 18 °C by water cooling, and was mostly run on 0.25 W output power. A reflection grating in combination with an aperture and lenses was used to remove laser noise and an unwanted laser peak at 810 nm, thereby increasing the quality of the laser beam. Further, a power controller was used to control the

intensity of the laser beam hitting the sample. The power controller consists of several plates of different attenuation which in different combinations produces a wide range of different attenuation factors in the beam path. Also a rotational plate with a constant gradient in attenuation was used to fine tune the laser intensity.

For polarization dependent measurements, polarization controller 1 (PC1) and polarization controller 2 (PC2) was used in two different sets of measurements. In the first set, the polarization dependence of the nanowire emission was measured. This was done by using a linear polarizer followed by a quarter wave plate (QWP) rotated at 45º for PC1, thereby exciting the nanowire with circular polarization and ensuring that the intensity of the laser beam was equal in every angle of polarization. PC2 consisted of a half wave plate (HWP) for the proper wavelength region rotated at angles from -60º to 60º with 5º intervals, followed by a linear polarizer. The HWP rotates linear polarization by twice the angle of it's own rotation from the linear polarizer. In this way, the linearly polarized PL intensity from the nanowire was measured from -120º to 120º with 10º intervals, thereby redundantly covering more than 180º.

In the second set of polarization measurements, PC1 consisted of a linear polarizer and a HWP for 532 nm while PC2 consisted of a QWP rotated at 45º to the following linear polarizer. The HWP in PC1 was rotated from -60º to 60º with 5º intervals in the same manner as for the first set. This was done to measure the rotation of the nanowire compared to the spectrometer. When the HWP was rotated so that the linear polarization was parallel to the nanowire, excitation would be at it's highest, and therefore also PL intensity. PC2 ensured that any linear polarization, regardless of rotational angle, resulted in the same intensity sent to the spectrometer.

After PC1, a beam splitter (BS) was used to couple the laser into the optical path of the sample, while a flip-away mirror was used route the sample beam either to a camera for real-time monitoring or to the spectrometer for spectroscopy measurements. Another BS was used to couple visible light into the optical path of the beam when real-time monitoring of the sample was necessary. A microscope objective was used to focus the laser and camera image on the sample surface. Laser beam intensity was measured in front of the microscope objective for power dependence measurements. Finally a lens matching the numerical aperture (NA) of the spectrometer was used to focus the emission beam into the spectrometer, and a selection filter blocked the 532

nm wavelength from entering the spectrometer. The spectrometer divided the emission beam into an emission spectrum as described in 3.1.2 and routed it to the Newton EMCCD. The CCD was supposed to be cooled to -70° C for all measurements. However, because of problems encountered with the cooling of the CCD, the only stable cooling temperature for the last half of the measurements was -55° C.

4. Results

4.1 PL of nanowires with and without AlGaAs shell
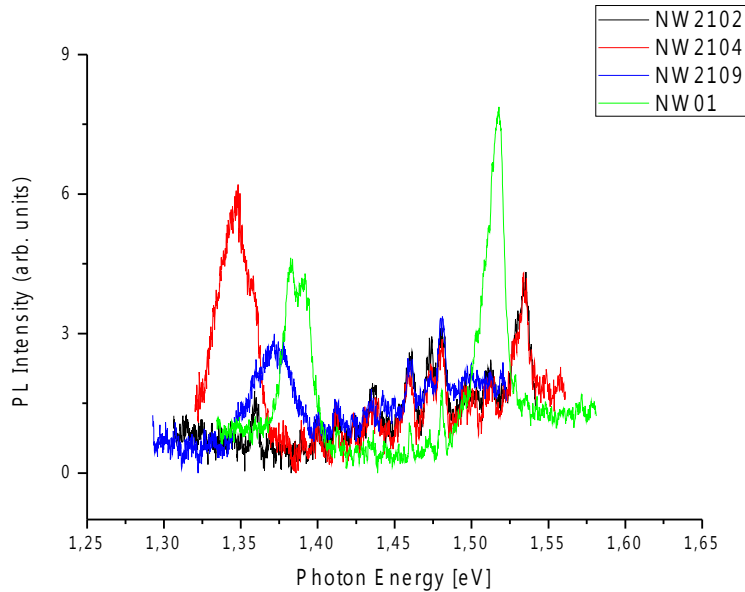
Figure 4.1.1. µ-PL measurements of NW2102, NW2104 and NW2109 from sample
As530-1 and NW01 from sample As530-2 with 50 µW laser power at 10 K.

Figure 4.1.1 shows the PL measurements of three nanowires from sample As530-1 and one nanowire from As530-2. These samples are GaAs nanowires with GaAsSb inserts, but without an AlGaAs shell. Figure 4.1.2 shows PL measurements of four nanowires from sample LPN2-4, which is the same structure of GaAs with a GaAsSb insert, but with an AlGaAs shell. As seen in the figures, the peaks around 1.3 to 1.4 eV are much broader and at higher energy levels for the nanowires with an AlGaAs shell. The peaks around 1.5 eV are also broader in the AlGaAs shell wires, while the photon energy of the peak seems to vary slightly for the nanowires without shells. Furthermore, the AlGaAs shell nanowires show emission peaks around 1.6 eV that are not present in the samples of nanowires without a shell. The PL measurements were carried out under the same conditions, and it is evident that the emission from the nanowires in Figure 4.1.2 is much stronger than the emission from Figure 4.1.1.
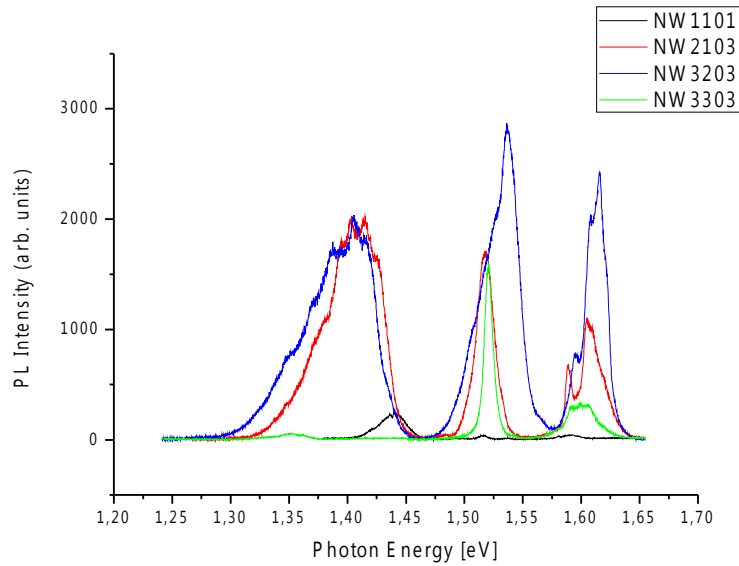
Figure 4.1.2. µ-PL measurements of NW1101, NW2103, NW3203 and NW3303 from sample LPN2-4 with 50 µW laser power at 10 K.

4.2 Sample As539-3 PL power dependence

Ten nanowires from sample As539-3, NW01 through NW10, was subjected to power dependent PL spectroscopy. These were AlGaAs nanowires with GaAs inserts, and showed characteristic peaks ranging from 1.511 eV to 1.53 eV, from 1.558 eV to 1.575 eV and from 1.633 eV to 1.668 eV. NW01 through NW08 and NW10 all showed these characteristic peaks, although NW07 and NW10 did not show peaks around 1.65 eV. NW05 has been chosen to represent these nanowires, and the PL measurements of this wire is presented in Figure 4.2.1. NW09 stood out from the rest of the nanowires measured in this sample by having a peak at 1.482 eV that blue shifted towards 1.52 eV, as shown in Figure 4.2.2.

Figure 4.2.1 shows the PL measurements of NW05. For low laser excitation power, it showed very small peaks at 1.462 eV, 1.482 eV, 1.668 eV and 1.713 eV, as well as slightly greater peaks at 1.522 eV, with a 6 meV lower energy shoulder, and at 1.562 eV. All these peaks were quite narrow, with an approximate FWHM of 2 meV. As laser excitation power increased, only the 1.522 eV, 1.562 eV and 1.668 eV peaks grew. The 1.522 eV and 1.562 eV peaks stayed narrow, but the 1.668 eV peak broadened significantly. While there was no blue shift, a peak at 1.530 eV appeared at the 1.522 eV peak, and the 1.562 eV peak appeared to red shift 9.5 meV as a new peak appeared at 1.565 (also slightly red shifting). For the highest laser excitation power, a peak at 1.571 eV appeared as a

shoulder on the 1.565 eV peak.
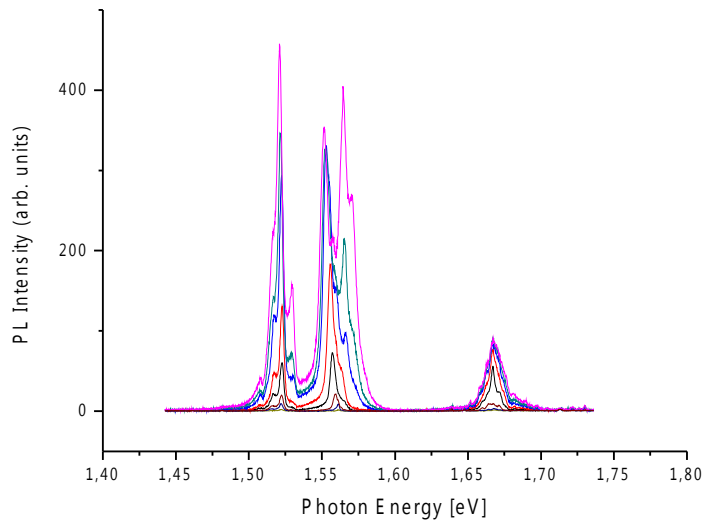
Figure 4.2.1. µ-PL measurements of NW05 of sample As539-3 at 14 K from 100 nW to 75 µW laser excitation power.

(a)	(b)
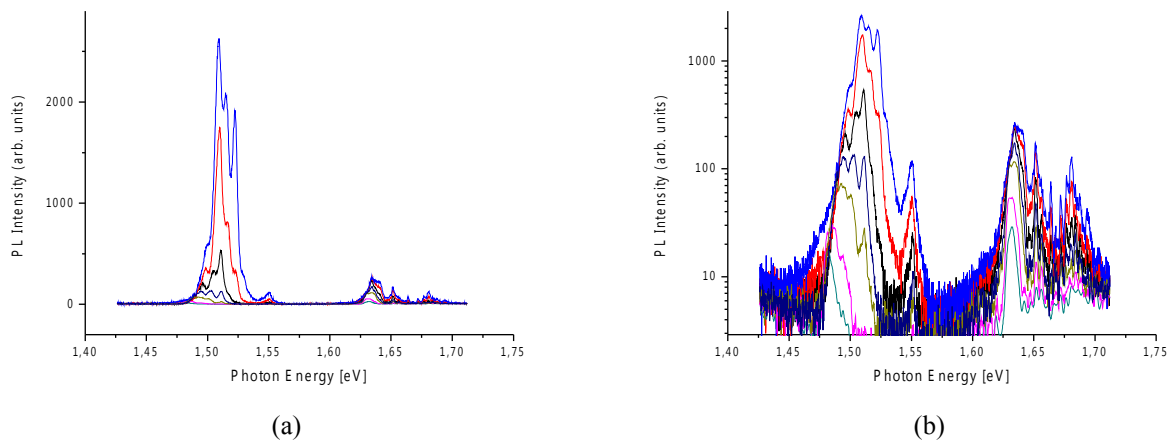
Figure 4.2.2. µ-PL measurements of NW09 of sample As539-3 at 10 K from 50 nW to 5 µW laser excitation power with (a) linear Intensity scale and (b) logarithmic Intensity scale.

Figure 4.2.2 shows the PL measurements of NW09 from sample As539-3. For low laser excitation power, two peaks with a 7.5 meV FWHM are visible at 1.482 eV and 1.632 eV. As laser power increased, the 1.482 eV peak immediately broadened and started to blue shift. For medium excitation power, the peak seemed to be consisting of several narrow peaks shifting emission power from lower to higher energy levels. The 1.632 eV peak did not broaden or blue shift, but several higher energy peaks with low emission power appear from 1.65 eV to 1.68 eV. For higher excitation power, the 1.482 eV peak appeared to blue shift to a main peak at 1.509 eV with a higher energy shoulder at 1.516 eV. Also, a high intensity peak at 1.522 eV appeared, along with a lower intensity peak at 1.55 eV.

4.3 Effects of STEM and TEM on nanowire PL
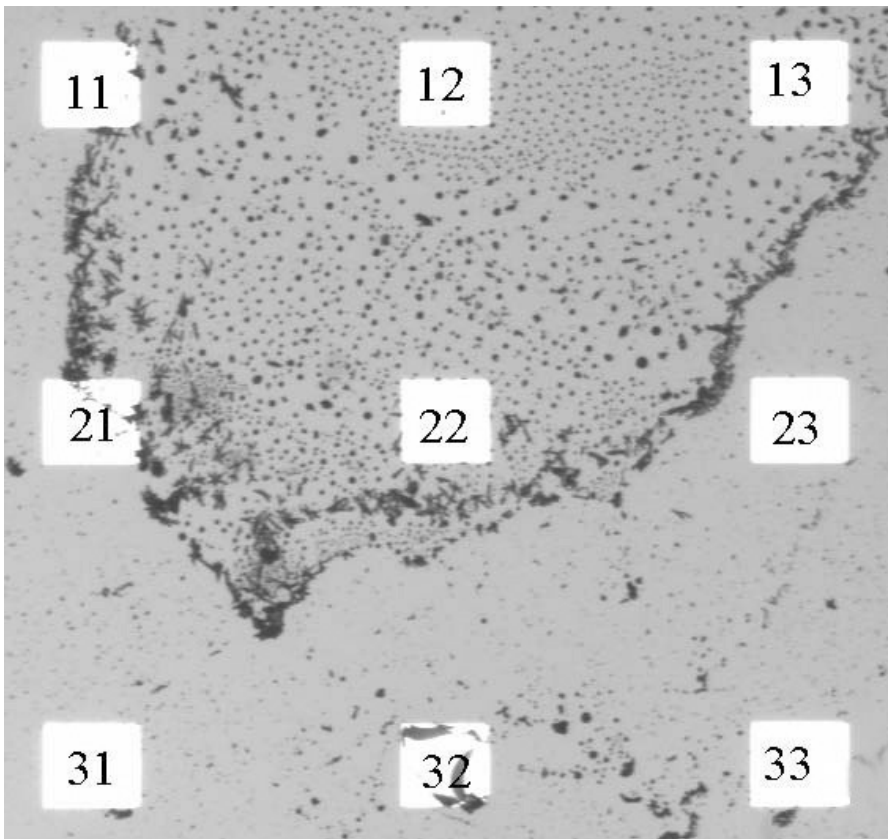
Figure 4.3.1. An optical image of sample LPN2-4 for PL-STEM-PL-TEM-PL correlated experiments.

In order to examine the effect of an electron beam in STEM and TEM on the optical properties of a nanowire, an experiment involving nanowires from sample LPN2-4 was defined. These nanowires with a GaAs/AlGaAs core/shell and GaAsSb insert structure were dispersed onto a sample consisting of nine windows of Si_3N_4-membranes of roughly 50 nm thickness. The windows were named from 11 to 33 as shown in Figure 4.3.1. By optical imaging, three to four promising nanowires were mapped in each window, and given names from NW1101 to NW3303, where the first two digits corresponds to the window the nanowire was situated in, and the last two corresponds to the specific name of a nanowire in this window. By preparing the sample in such a manner, it was possible to examine individual nanowires in μ-PL spectroscopy followed by STEM, μ-PL spectroscopy, TEM and again μ-PL spectroscopy, since the electron beam would easily penetrate the 50 nm thick membrane in TEM.

It was decided that window 31, 32 and 33 would be reference windows, and would never be hit by an electron beam. By doing this, it would be safe to assume that any change observed in μ-PL of row one and two that did not take place in row three must be caused by the electron beam. It was

also decided that the different windows in rows one and two would be imaged with an electron beam with varying acceleration voltage in STEM, in order to examine if there is any threshold acceleration voltage to safely image nanowires without causing damage. Therefore, the electron beam acceleration voltage was 5 kV, 10 kV, 15 kV, 20 kV, 25 kV and 30 kV for window 11, 12, 13, 23, 22 and 21 respectively.

The first μ-PL measurements were conducted on March 16th, while the STEM images were taken on March 19th. The second set of μ-PL measurements were measured on March 22nd, while the TEM imaging of the sample was conducted from March 23rd to May 19th. The last set of μ-PL measurements were taken on May 21st. After the STEM imaging, neither the electron beam irradiated nor the reference nanowires showed any dramatic change in PL. However, after TEM, the imaged nanowires displayed no or extremely low PL, while the reference nanowires in row three still displayed quite strong PL. In this section NW1202, NW2103 and NW2302 are presented as examples of electron beam irradiated nanowires, while NW3101 and NW3203 are presented as reference nanowires. A total STEM and TEM induced PL change review of the LPN2-4 sample can be found in Appendix A.
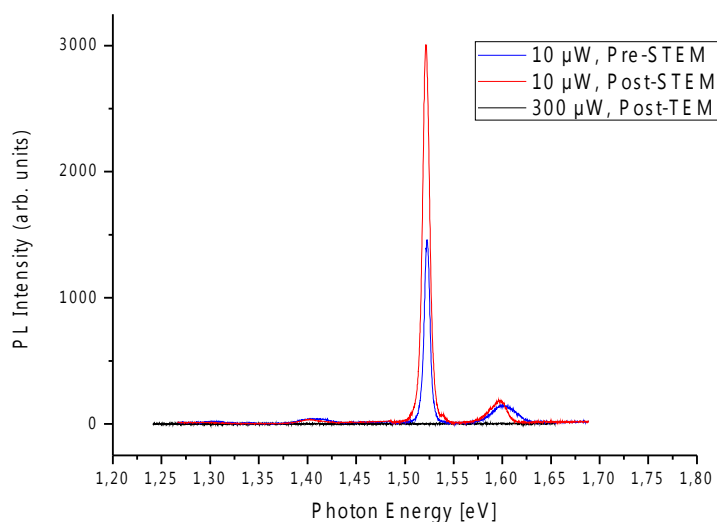
Figure 4.3.2. μ-PL measurements of NW1202 of sample LPN2-4 before and after 10 kV STEM imaging and after 200 kV TEM imaging for specified laser excitation power.

Figure 4.3.2 shows specific μ-PL measurements of NW1202 before and after STEM imaging at 10 kV acceleration voltage, and after TEM imaging at 200 kV. Before STEM, NW1202 showed a weak and broad peak at 1.305 eV which was much more difficult to observe at the same laser excitation

power after STEM. The slightly stronger peak at 1.404 eV was not changed much, although it appeared slightly weaker after STEM. The sharp and strong 1.522 eV peak appeared twice as strong after STEM, and was shifted 1 meV down from the pre-STEM measurements. The 1.602 eV peak seemed approximately as strong before and after STEM, but was shifted 2 meV down. The μ-PL measurements after TEM did not show any peaks, despite 30 times stronger laser excitation power.
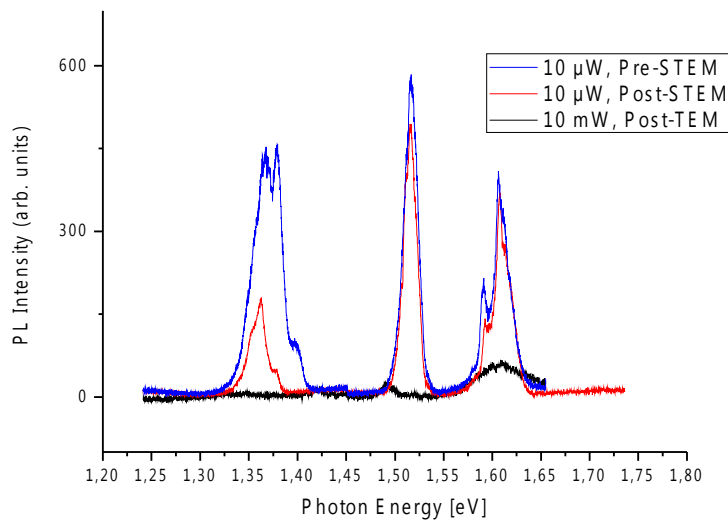
Figure 4.3.3. μ-PL measurements of NW2103 of sample LPN2-4 before and after 30 kV STEM imaging and after 200 kV TEM imaging for specified laser excitation power.

Figure 4.3.3 shows specific μ-PL measurements of NW2103 before and after STEM imaging at 30 kV acceleration voltage, and after TEM imaging at 200 kV. There was neglectable difference in the 1.516 eV and the 1.606 eV peaks before and after STEM. After TEM the peaks were extremely weak, and the 1.516 eV peak is shifted to a 24 meV lower energy level while the 1.606 eV peak was significantly broader. The 1.367 eV peak was almost reduced by a factor of 2.5 from pre-STEM to post-STEM, and was at a 5 meV lower energy level. After TEM at 10 mW laser excitation power, there was only a hint of a peak at 1.421 eV.
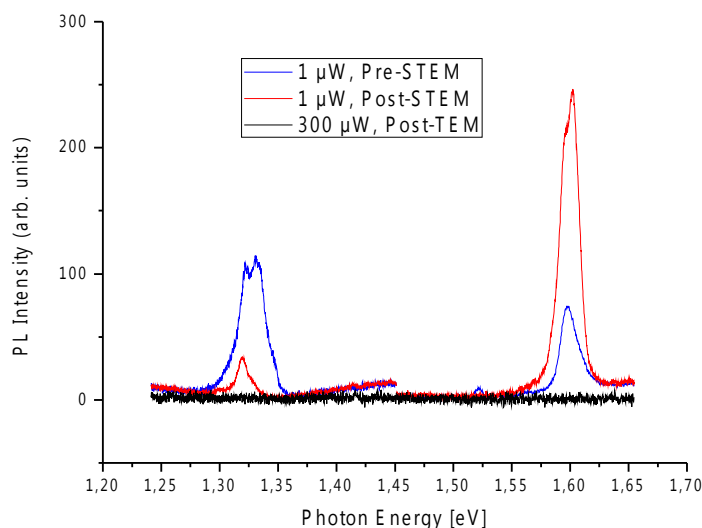
Figure 4.3.4. μ-PL measurements of NW2302 of sample LPN2-4 before and after 20 kV STEM imaging and after 200 kV TEM imaging for specified laser excitation power.

Figure 4.3.4 shows specific μ-PL measurements of NW2302 before and after STEM imaging at 20 kV acceleration voltage, and after TEM imaging at 200 kV. While the peak at 1.322 eV was at a 3 meV lower energy level and was reduced by more than a factor of 3.6 in intensity, the 1.598 eV peak was shifted 4 meV up and was more than 3.3 times stronger in intensity before and after STEM. Before STEM, a peak at 1.522 eV was barely visible at 1 μW laser excitation power, but after STEM, the peak was not observable until a higher laser power was reached. After TEM, no peaks were observed despite 300 times greater laser excitation power.
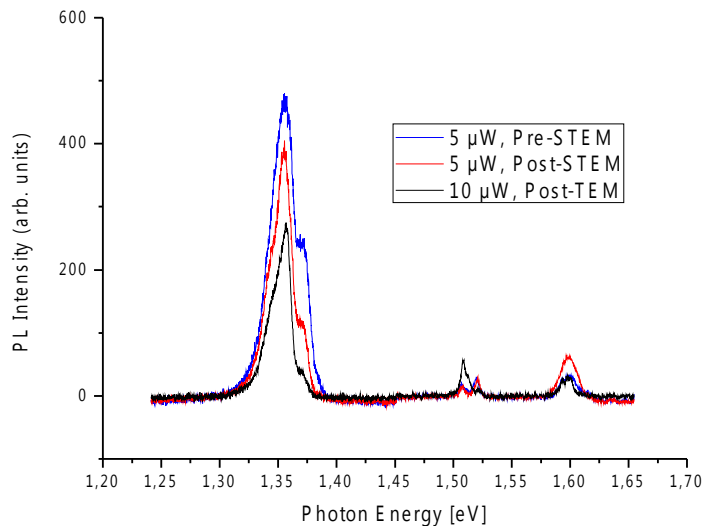
Figure 4.3.5. µ-PL measurements of NW3101 of sample LPN2-4 before and after STEM and TEM imaging without electron beam radiation for specified laser excitation power.

Figure 4.3.5 shows specific µ-PL measurements of NW3101 before and after STEM and TEM imaging of other nanowires without the electron beam hitting NW3101. Although there was practically no shift in energy levels of the emission peaks, the 1.598 eV peak was twice as strong after STEM as compared to before. There was no difference in the 1.507 eV and 1.520 eV peaks before and after STEM, but the 1.355 eV peak was slightly weaker. After the TEM sessions, the peaks were still quite strong at low laser excitation powers, unlike the nanowires radiated with the electron beam. The 1.355 eV peak seemed to be blue shifted 1 meV, despite an emission intensity reduction of a factor of approximately 2 at twice the laser excitation power. Also the 1.598 eV peak showed a strong reduction in intensity, but the peak was not shifted in energy. While the 1.520 eV peak was almost non existent in the µ-PL measurements post-TEM, the 1.598 eV peak was stronger and seemed to be shifted 1 meV up in emission peak energy level.
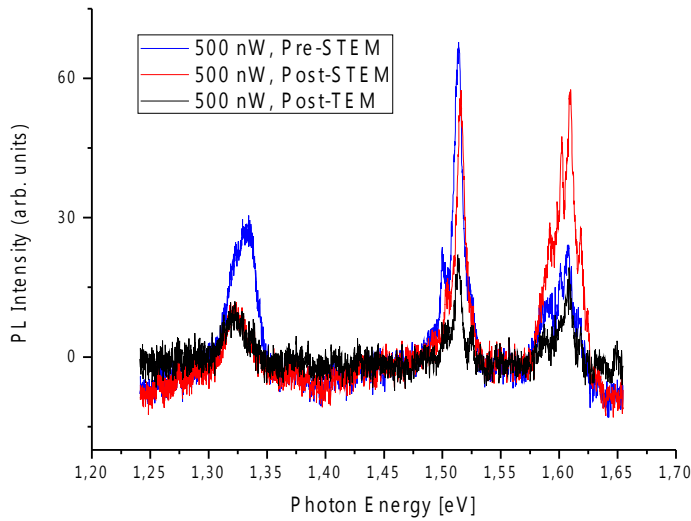
Figure 4.3.6. μ-PL measurements of NW3203 of sample LPN2-4 before and after STEM and TEM imaging without electron beam radiation for specified laser excitation power.

Figure 4.3.6 shows specific μ-PL measurements of NW3203 before and after STEM and TEM imaging of other nanowires without the electron beam hitting NW3203. Also NW3203 showed an increase in 1.607 eV peak intensity after STEM, while the 1.514 eV peak was slightly weaker and seemed to be shifted 2 meV up in energy. After TEM, the 1.514 peak shifted back 2 meV to the original peak energy value, but the peak intensity was much weaker. Also, after TEM the 1.607 eV peak had weakened to slightly below the pre-STEM measurement. The 1.332 eV peak weakened to approximately one third of the pre-STEM measured peak after STEM, and shifted down nearly 10 meV, but there was no significant difference for this peak between post-STEM and post-TEM.

4.4 Optically and structurally correlated examination of LPN2-4

In this section μ-PL measurements for selected nanowires from sample LPN2-4 will be presented along with TEM images of the specific nanowires. Of the 29 nanowires mapped for optical and structural examination, 18 wires showed strong blue shifting of peaks ranging from 1.3 eV to 1.4 eV. The blue shifting of these peaks appeared to be not only a shift of the entire peak towards higher energy, but also higher energy peaks within the main peak reaching higher emission intensity than lower energy peaks, as will be shown in the following four figures. To represent this majority category of nanowires, NW2302 and NW1102 was chosen.

*Figure 4.4.1. Power dependent µ-PL measurements of NW2302 of sample
LPN2-4 at 10 K from 500 nW to 30 µW laser excitation power.*

Figure 4.4.1 shows the µ-PL measurement of NW2302. At low laser excitation power a broad peak at 1.321 eV with a FWHM of 19 meV, a weak peak at 1.522 eV and a broad peak at 1.599 eV with a 18 meV FWHM was observable. As laser power increased, the 1.522 eV peak grew slightly stronger, and broadened to a 6 meV FWHM, while the 1.599 eV peak blue shifted to 1.605 eV and broadened to 21 meV FWHM. The 1.321 eV peak grew much stronger, broadened and blue shifted to 1.405 eV. At higher laser powers, this blue shifting appeared to consist of both shifting of the main peak to higher energy levels, as well as lower energy peaks being consumed by higher energy peaks inside the main peak envelope.
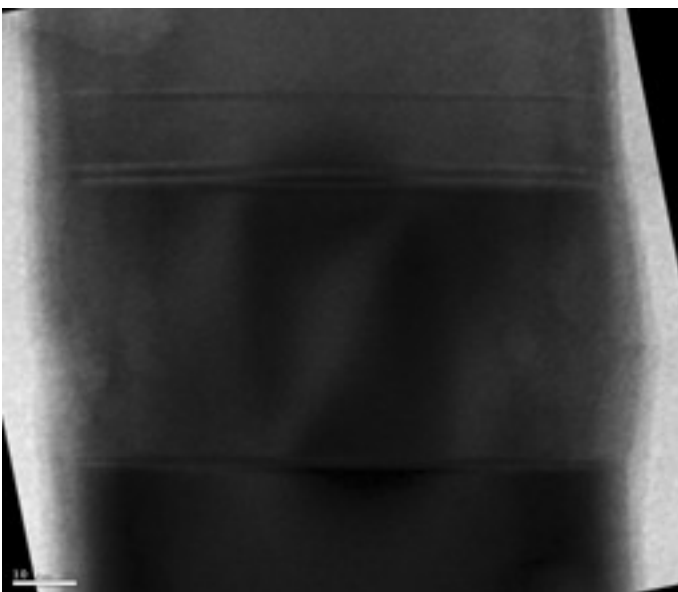
*Figure 4.4.2. TEM image of the GaAsSb insert in NW2302 at
81k magnification.*

Figure 4.4.2 shows a TEM image of the insert in NW2302. As seen in the figure, two short stacking faults of ZB GaAs are quite close to the insert, but there are no twin defects in the insert.
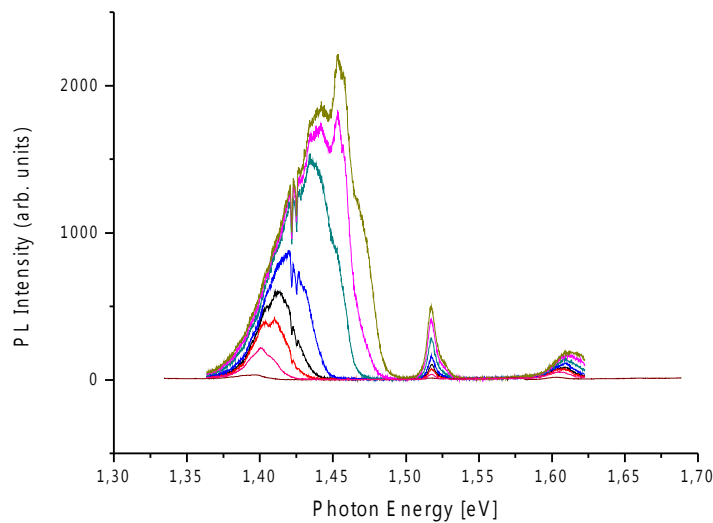
Figure 4.4.3. Power dependent µ-PL measurements of NW1102 of sample LPN2-4 at 10 K from 100 nW to 10 µW laser excitation power.

Figure 4.4.3 shows the µ-PL measurement of NW1102. At low laser power, a peak at 1.398 eV with a 25 meV FWHM was visible along with a weak peak at 1.518 eV and a slightly stronger peak at 1.603 eV with a 15 meV FWHM. As laser power increased, the 1.603 eV peak broadened and grew slightly, while the 1.518 eV peak grew without much broadening. The 1.398 eV peak grew considerably, and blue shifted to 1.454 eV by the same procedure as described for NW2302. The sharp PL aberrations observed at 1.422 eV and 1.425 eV were caused by pixel error in the EMCCD that changed along with spectrometer central wavelength.
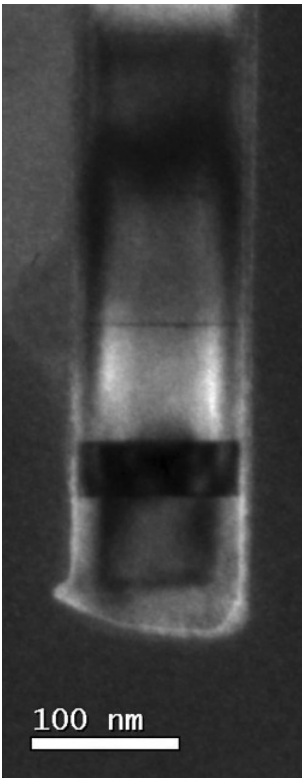
Figure 4.4.4. TEM image of the GaAsSb insert in NW1102 at 17k magnification.

Figure 4.4.4 shows the TEM image of NW1102. It shows a quite clean insert, with a distance of almost 100 nm to the closest stacking fault. However, it also shows that the wire was broken off less than 100 nm below the insert.

Figure 4.4.5. Power dependent μ-PL measurements of NW1302 of sample LPN2-4 at 10 K from 350 nW to 50 μW laser excitation power.

Figure 4.4.5 shows the μ-PL measurement of NW1302. At low laser power, a 15 meV FWHM peak was visible at 1.319 eV, along with weak peaks at 1.488 eV, 1.501 eV and 1.605 eV. As laser power increased, the 1.501 eV peak grew much stronger than the 1.488 eV peak and red shifted 7 meV,

while the 1.605 eV peak broadened and grew slightly. The 1.319 eV peak blue shifted to 1.397 eV by the same procedure as for NW1102 and NW2302.
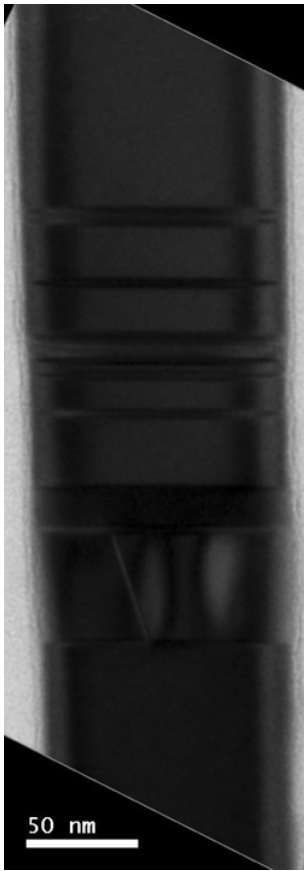
Figure 4.4.6. TEM dark field image of the GaAsSb insert in NW1302 at 31k magnification.

Figure 4.4.6 shows a TEM image of the insert in NW1302. Below the insert, there were no stacking faults nearby. In the insert, there was a twin defect slightly skew compared with the nanowire axis. Directly above the insert, there was a region of 4H polytypism of GaAs, followed by several stacking faults of ZB GaAs in otherwise WZ GaAs.
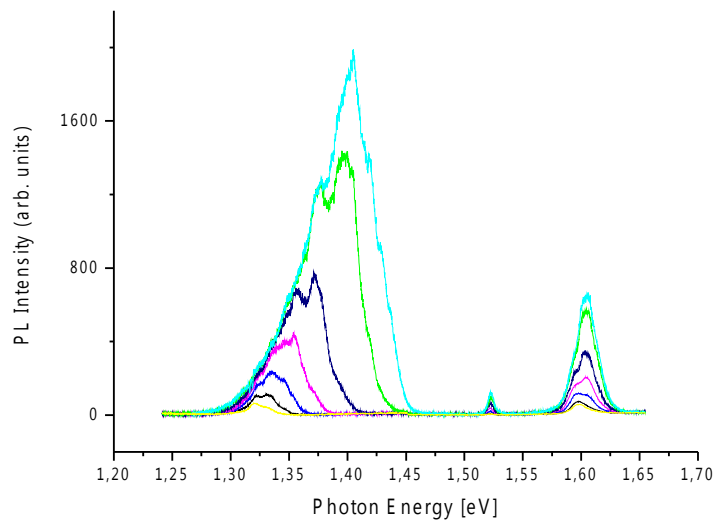
Figure 4.4.7. Power dependent µ-PL measurements of NW2101 of sample
LPN2-4 at 10 K from 100 nW to 20 µW laser excitation power.

Of the 29 nanowires measured of the LPN2-4 sample, not all wires showed the blue shift procedure described by NW2302, NW1302 and NW1102. Of the five nanowires that showed a continuous broad peak energy blue shift, NW2101 was chosen to represent this category. Figure 4.4.7 shows the µ-PL measurement of NW2101. At low laser power, a peak at 1.368 eV with a 25 FWHM was observable along with a peak at 1.496 eV with a 5 meV FWHM and a shoulder peak at 1.502 eV. As laser power increased, the 1.502 eV peak grew stronger than the 1.496 eV peak before it blue shifted to 1.511 eV. The 1.368 eV peak blue shifted to 1.433 eV by continuous peak shifting without observable sub peak shifting as seen in NW2302, NW1302 and NW1102.
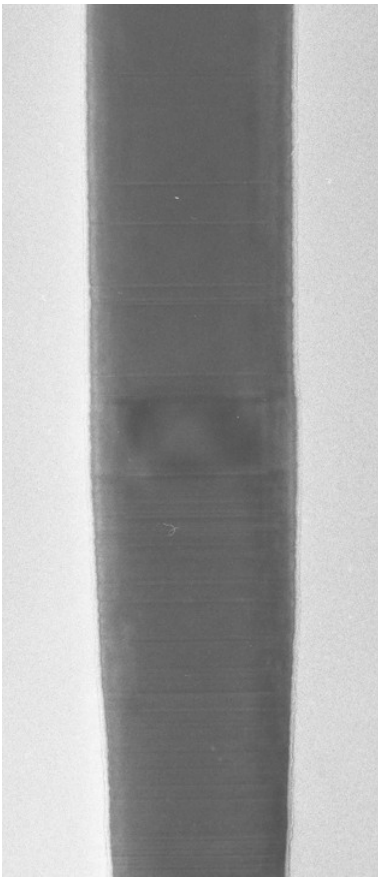
Figure 4.4.8. TEM image of NW2101 taken without CCD.

Figure 4.4.8 shows a TEM image of NW2101. Because problems were encountered using the normal CCD camera in the TEM, the image has been taken with regular film. Therefore, there is no calibrated scale visible in the image. However, the image still shows several short stacking faults of ZB GaAs in WZ GaAs below and above the insert.
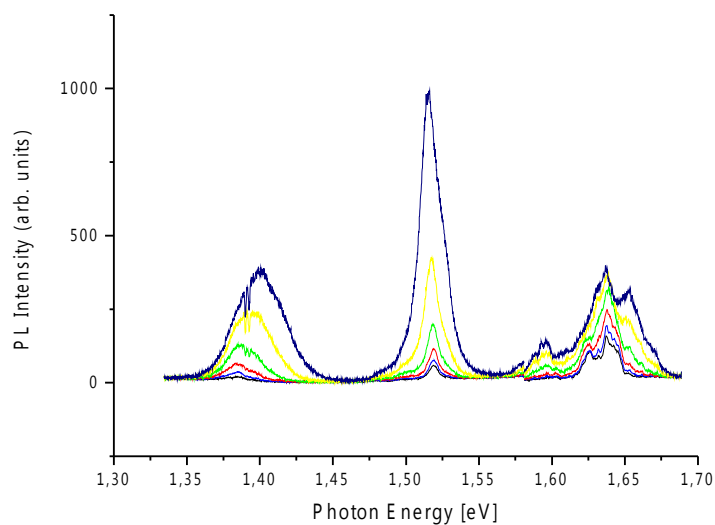
Figure 4.4.9. Power dependent μ-PL measurements of NW1103 of sample LPN2-4 at 10 K from 10 μW to 200 μW laser excitation power.

Of the 29 nanowires in the measurement set, three nanowires showed less blue shifting than other nanowires, despite still relatively strong peak emission intensity. NW1103 and NW1203 was chosen to represent this category of nanowires. Figure 4.4.9 shows the μ-PL measurement of NW1103. At low laser power, a weak peak at 1.384 eV was observable along with a stronger peak at 1.519 eV and a set of three peaks around 1.63 eV. As laser power increased, the 1.63 eV peaks grew in both strength and complexity. The 1.519 eV peak grew significantly and red shifted 2 meV, while the 1.384 eV peak blue shifted only 15 meV despite a significant increase in emission intensity.
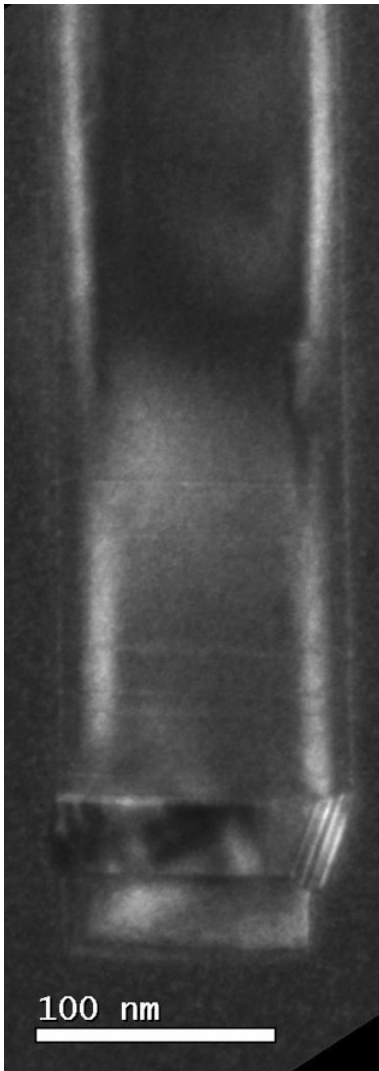
Figure 4.4.10. TEM image of NW1103 at 21k magnification.

Figure 4.4.10 shows a TEM image of NW1103. As shown in the figure, NW1103 was broken quite close below the insert. In the insert, there were multiple twin defects skewed on the right side as the nanowire diameter increased from bottom insert to top insert. Above the insert, four short stacking faults were visible close to the insert.
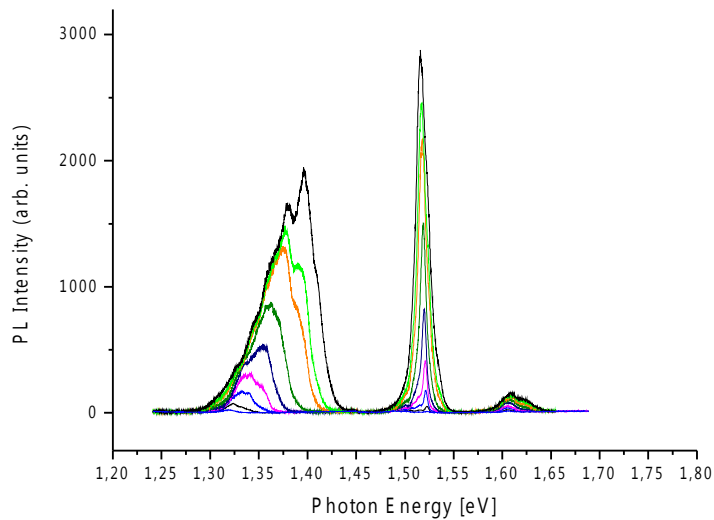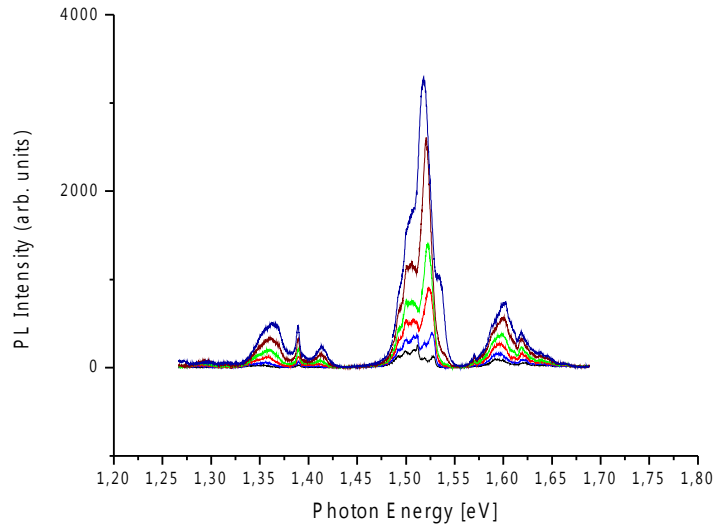
Figure 4.4.11. Power dependent μ-PL measurements of NW1203 of sample LPN2-4 at 13 K from 5 µW to 75 µW laser excitation power.

Figure 4.4.11 shows the μ-PL measurement of NW1203. At low laser power, a broad peak of 28 meV FWHM was visible at 1.349 eV along a sharper peak at 1.390 eV. At 1.51 eV, a peak interval was observed with peaks at 1.492 eV, 1.499 eV, 1.509 eV, 1.512 eV, 1.519 eV and 1.529 eV with the 1.512 eV peak being the main peak. Also, a broad peak at 1.593 eV was observed along with a peak at 1.622 eV. As laser power increased, the 1.529 eV peak grew faster than the surrounding peaks, and red shifted to 1.518 eV. The 1.349 eV peak blue shifted to 1.363 eV, and a peak at 1.409 eV appeared and blue shifted 5 meV. The 1.390 eV peak did not blue shift or broaden, but grew in strength.

Although NW1203 represents nanowires with little blue shift of peaks around 1.4 eV, it also represents nanowires with a sharp peak around 1.4 eV that seemed slightly out of place. This peak was observed in NW1203 and NW2201.
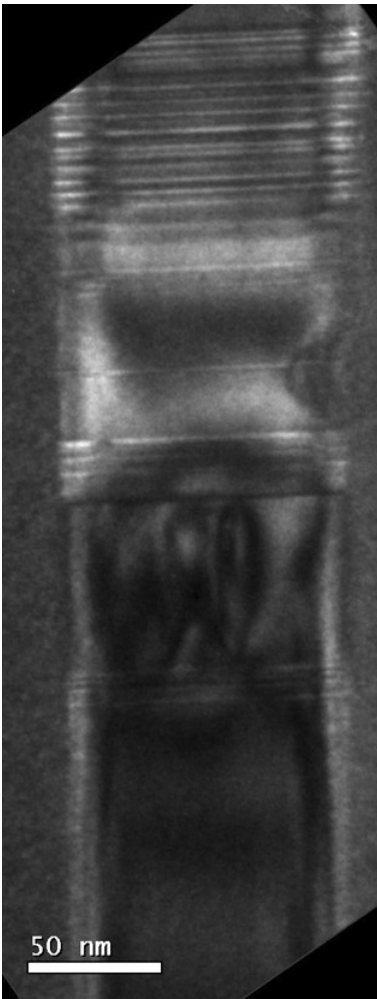
Figure 4.4.12. TEM image of NW1203 at 31k magnification.

Figure 4.4.12 shows a TEM image of NW1203. Stacking faults were visible quite close both above and below the insert. The insert itself contained no twin defects. Above the insert and the nearby stacking faults, there was a region of mostly WZ followed by a region of many stacking faults.
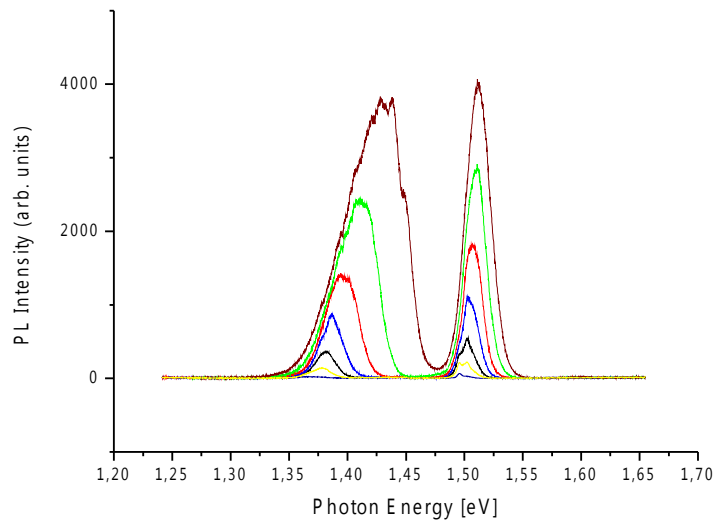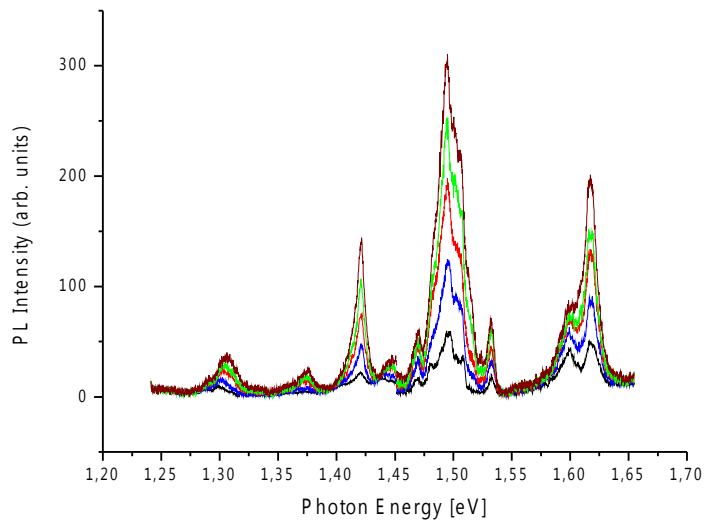
*Figure 4.4.13. Power dependent µ-PL measurements of NW2201 of sample
LPN2-4 at 10 K from 10 µW to 50 µW laser excitation power.*

Figure 4.4.13 shows the µ-PL measurement of NW2201. At low laser power, weak peaks were observable at 1.299 eV, 1.420 eV, 1.439 eV, 1.469 eV, 1.533 eV, 1.601 eV and 1.616 eV along with a stronger peak at 1.495 eV with shoulder peaks at 1.480 eV and 1.507 eV. As laser power increased the 1.420 eV, 1.495 eV and 1.616 eV peaks grew stronger than the other peaks. No blue shift or red shift was observed for the three main growing peaks.

(a)   (b)
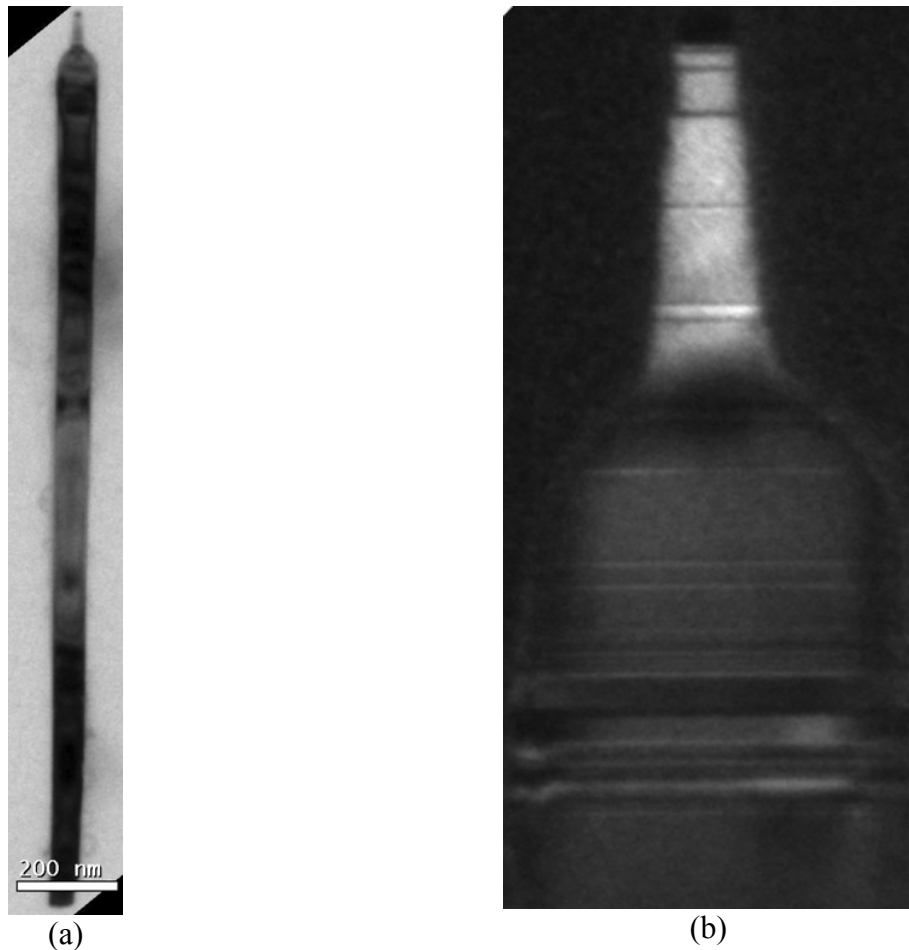
Figure 4.4.14. TEM image of NW2201 at 5.6k(a) and 42k(b) magnification.

Figure 4.4.14 shows a TEM image of the entire NW2201. As seen in the figure, there was no GaAsSb insert in this nanowire. The tip, however, displayed both twins in ZB regions of GaAs, 4H GaAs and several short stacking faults.

4.5 PL of WZ versus ZB GaAs

While the LPN2-4 sample was in TEM sessions, PL measurements were conducted on NW01 through NW07 and NW01 through NW06 of sample As540-8 and As540-9, respectively. Both As540-8 and As540-9 are GaAs core nanowires with a GaAsSb insert and an AlGaAs shell. However, there is still a difference between these samples. In As540-8 the GaAs had the WZ structure, while in sample As540-9, the GaAs was ZB. The GaAsSb insert was ZB for both samples.

46
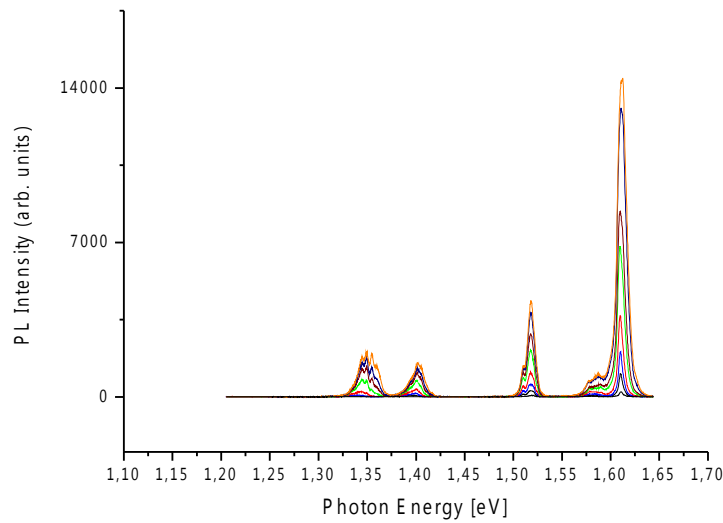
Figure 4.5.1. Power dependent μ-PL measurements of NW06 of sample As540-8 at 9 K from 500 nW to 50 μW laser excitation power.

Figure 4.5.1 shows the μ-PL measurements of NW06, which was the wire chosen to represent sample As540-8. At low laser power, weak peaks were visible at 1.330 eV, 1.381 eV and 1.580 eV. Stronger peaks were also visible, as there was a sharp peak at 1.611 eV with a 4 meV FWHM, and a peak at 1.520 eV with a 7 meV FWHM and a shoulder peak at 1.518 eV. As laser power increased, all peaks grew in intensity. The 1.518 eV peak and the 1.611 eV peak remained stable at their respective energy levels, but there was a weak blue shift observed for the 1.580 eV peak. The 1.330 eV peak blue shifted to 1.350 eV by what appeared to be discrete peaks of higher energy growing stronger than lower energy peaks in the main peak envelope, while the 1.381 eV peak blue shifted to 1.402 eV by a steady peak shift. NW06 was chosen to represent the As540-8 nanowires because the PL measurements of this wire displayed a low blue shift of two peaks between 1.3 eV and 1.4 eV in the same way as NW02 and NW03. NW04 and NW05 also showed a low blue shift, but of a single peak in the same region. NW01 and NW07 showed the same PL as most wires in LPN2-4, that being a single peak in the 1.3 eV to 1.4 eV region blue shifting in the area of 80 meV.
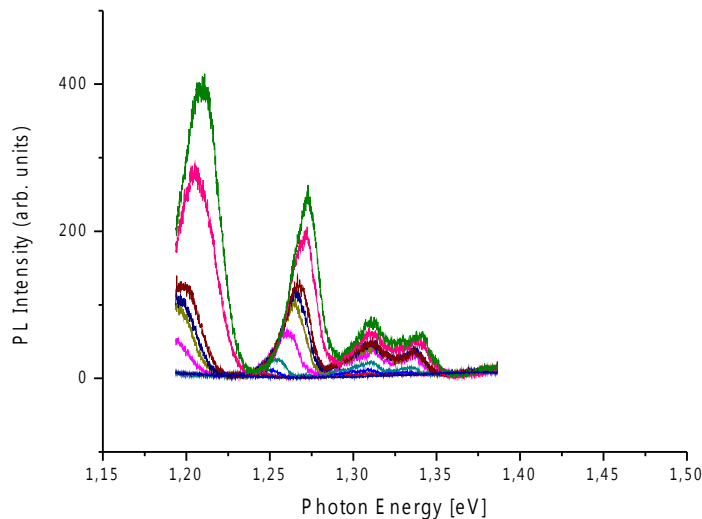
Figure 4.5.2. Power dependent µ-PL measurements centered at 960 nm of NW03 of sample As540-9 at 8 K from 500 nW to 100 µW laser excitation power.

Figure 4.5.2 shows the µ-PL measurements centered at 960 nm of NW03 of sample As540-9, which was the wire chosen to represent the nanowires measured of this sample. At the lowest laser excitation power, a weak peak was observable at 1.228 eV. As laser power increased, peaks at 1.306 eV and 1.329 eV appeared. As all the peaks blue shifted, a strong peak blue shifted into the spectrum range, perhaps originating from approximately 1.17 eV. Since the EMCCD used for this measurement did not cover photons of energy less than 1.18 meV, the origin of this peak had to be estimated by the amount of blue shift of the 1.228 eV peak. In total, the 1.228 eV peak blue shifted to 1.272 eV, while the 1.17 eV peak blue shifted to 1.210 eV. Although only slightly, the 1.306 eV and 1.329 eV peaks appeared to blue shift to 1.311 eV and 1.338 eV. NW03 was chosen to represent the rest of the wires because NW01 through NW06 of sample As540-9 showed a blue shifting peak around 1.22 eV, and peaks around 1.34 eV. NW03, however, also showed this higher intensity peak blue shifting from approximately 1.17 eV that was not observed in the other nanowires.
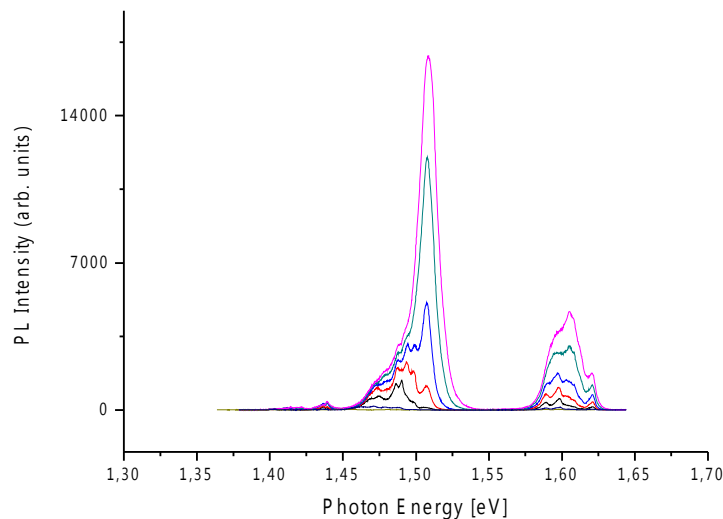
Figure 4.5.3. Power dependent μ-PL measurements centered at 820 nm of NW03 of sample As540-9 at 8 K from 500 nW to 50 μW laser excitation power.

Figure 4.5.3 shows the μ-PL measurements of NW03 of sample As540-9 centered at 820 nm. At low laser excitation power, a weak peak was visible at 1.402 eV along with two stronger peaks at 1.590 eV and 1.598 eV. Several peaks were observable in the region 1.428 eV to 1.502 eV, with a main peak at 1.447 eV. As laser power increased, the 1.402 eV peak did not grow nearly as much as the other peaks. The double peak around 1.595 eV merged into a single peak, and blue shifted to 1.608 eV, while the multiple peaks in the region of 1.45 eV merged into a single, broad peak that blue shifted to 1.508 eV. NW02 of sample As540-9 did not show strong peaks in the 1.5 eV region. Although NW01, NW04, NW05 and NW06 showed peaks in the same regions as NW03, the peaks around 1.45 eV did not blue shift to the area of 1.5 eV, but rather showed peaks at 1.5 eV simultaneously with blue shifting peaks from 1.45 eV. As in sample 540-8, peaks in the range 1.56 eV to 1.58 eV was observable in NW01 and NW06. NW06 also displayed two peaks of approximately 5 meV FWHM at 1.399 eV and 1.422 eV. As laser power increased, the 1.422 eV peak grew much stronger than the 1.399 eV peak and broadened towards higher photon energy. This peak can be seen at high laser excitation in Figure 4.6.4.

4.6 Polarization of nanowire PL
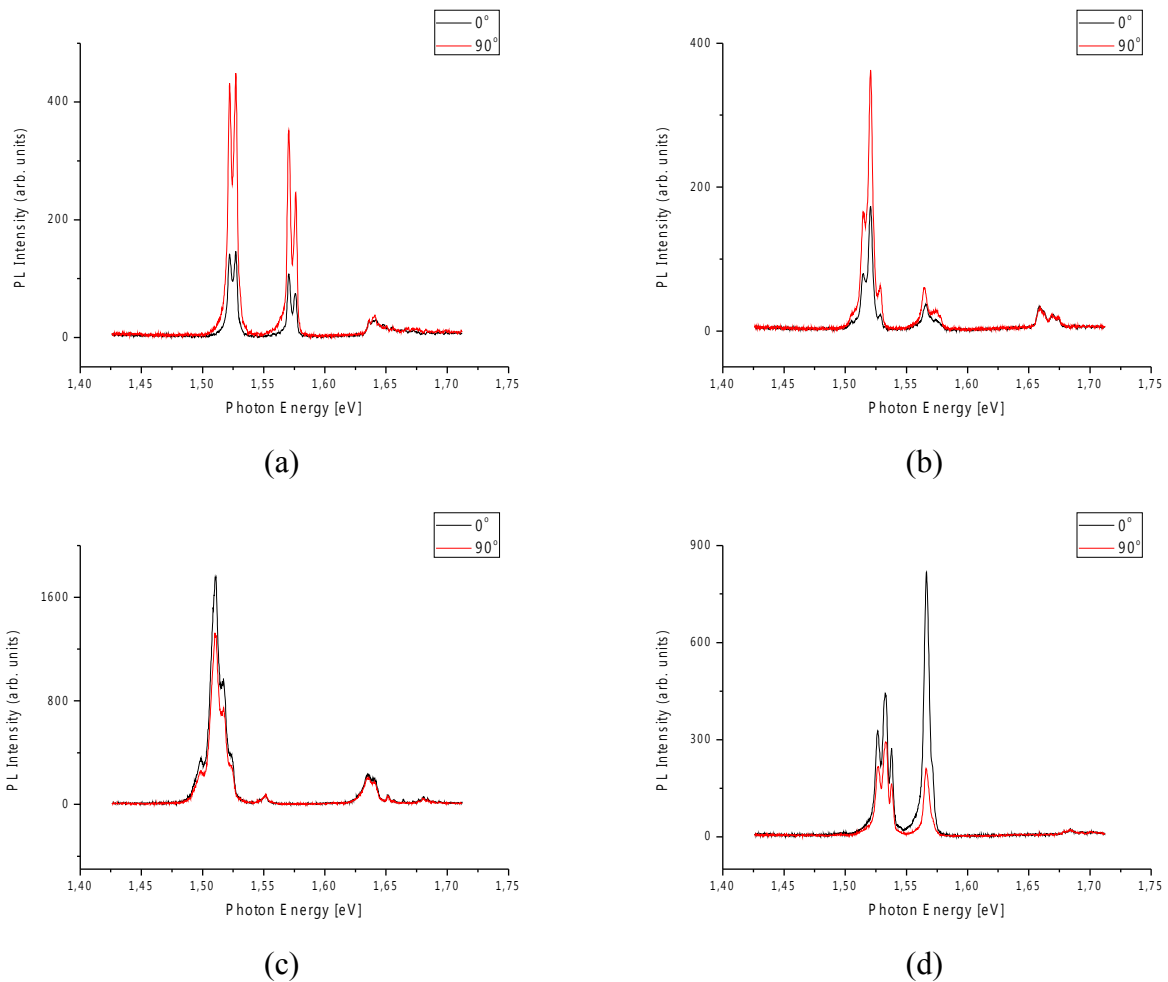
Figure 4.6.1. Polarization dependent μ-PL measurements of NW07(a), NW08(b), NW09(c) and NW10(d) of sample As539-3.

Figure 4.6.1 shows the polarization dependance of NW07 through NW10 of sample As539-3. The characteristic peak at 1.52 eV showed a polarization factor, P from (2), ranging from -51% to 20%, while the peak around 1.57 eV showed P ranging from -53% to 47%, and the peak around 1.65 eV -11% to 5% in the different nanowires.
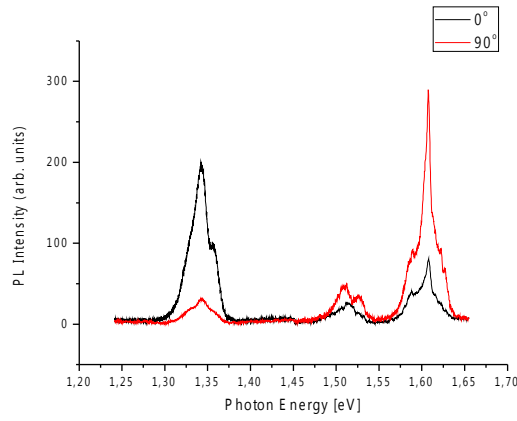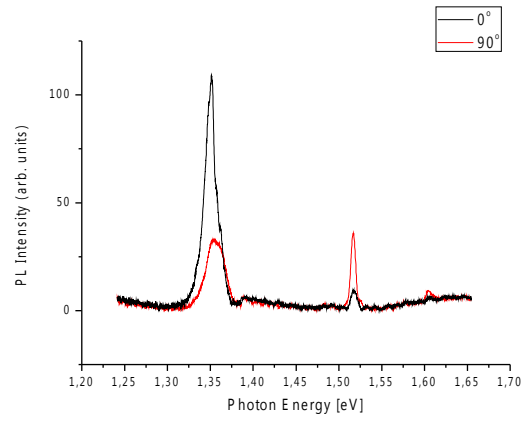
(a)   (b)

Figure 4.6.2. Polarization dependent μ-PL measurements of NW1303(a) and NW3103(b) of sample LPN2-4.

Figure 2.6.2 shows the polarization dependance of the μ-PL measurements of sample LPN2-4.

A polarization factor, P, of 73% and 53% are observable for the peaks at 1.35 eV in the two wires, while P was -30% and -58% for the peaks at 1.51 eV, and -57% and -13% for the peaks at 1.6 eV.
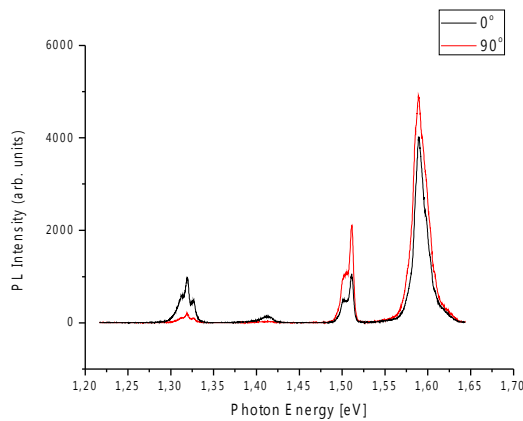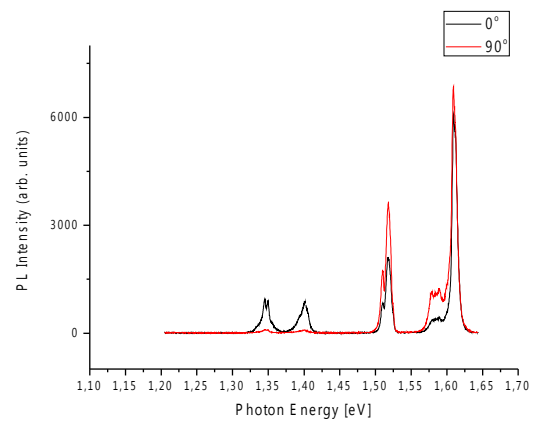
(a)   (b)
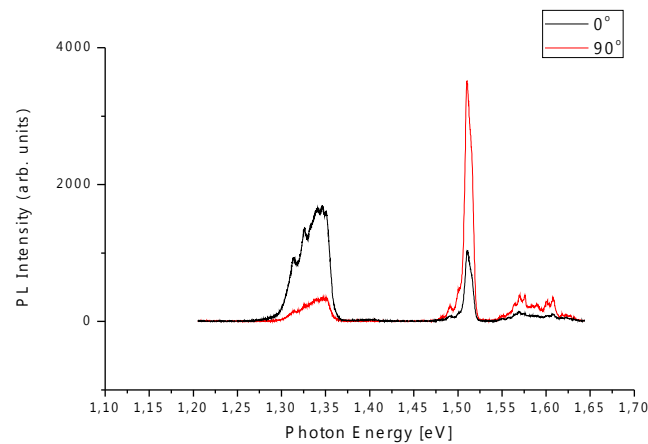
(c)

Figure 4.6.3. Polarization dependent μ-PL measurements of NW01(a), NW06(b) and NW07(c) of sample As540-8.

Figure 2.6.3 shows the polarization dependance of the µ-PL measurements of sample As540-8. The polarization factor observed for the different peaks ranged from 64% to 81% for the peaks at 1.35 eV, from -26% to -54% for the peaks at 1.52 eV and from -6% to -45% for the peaks at 1.6 eV.

(a)

(b)

(c)
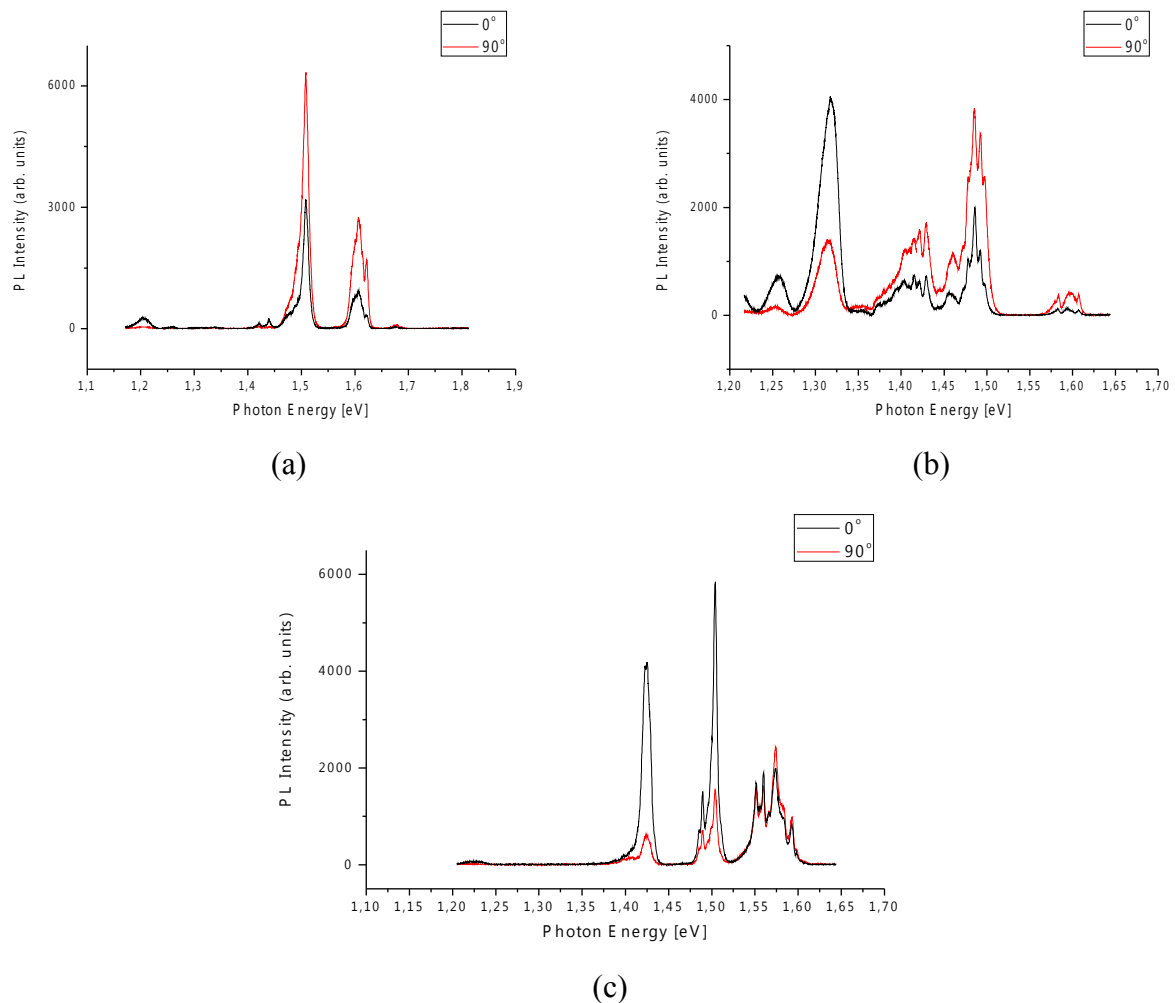
Figure 4.6.4. Polarization dependent µ-PL measurements of NW03(a), NW05(b) and NW06(c) of sample As540-9.

Figure 2.6.4 shows the polarization dependance of the µ-PL measurements of sample As540-9. For the peaks close to 1.2 eV, the observed polarization factor ranged from 60% to 73%. The peaks close to 1.4 eV displayed polarization factors at 100% and 75%, except for the complexity of peaks around 1.4 eV in NW05, which had a polarization factor of -33%. NW03 and NW05 displayed a polarization factor of -33% and -31% for the 1.5 eV peaks respectively, while NW06 displayed a polarization factor of 58% for this peak. The peaks at 1.6 eV showed polarization factors ranging from -10% to -55%.

5. Discussion

5.1 PL of nanowires with and without AlGaAs shell

Figure 4.1.1 and Figure 4.1.2 in section 4.1 showed the PL measurements at 50 µW laser excitation power of GaAs nanowires with GaAsSb inserts with and without an AlGaAs shell, respectively. By comparison of the two figures, it was obvious that the GaAsSb peak around 1.35 eV and GaAs peak around 1.52 eV were much stronger in the AlGaAs coated wires. Because the measurements of the samples presented in Figure 4.1.1 were conducted without the use of the diffraction grating showed in Figure 3.2.1, the small peaks observable in the region 1.42 eV to 1.55 eV were most likely attributed to laser noise. This would explain why these peaks were practically identical in peak position and intensity for different nanowires, and why these peaks were not observed in the rest of the measurements presented in this thesis as they were conducted with the diffraction grating in place.

Other than the intensity of the peaks, there was little difference in the GaAsSb peaks and GaAs peaks in the two figures. The GaAsSb peaks are broader and higher in energy in the AlGaAs coated wires. This was only natural as 50 µW corresponds to a very high excitation level for these wires, while 50 µW was usually the starting point of observable PL for nanowires without an AlGaAs shell, and the GaAsSb peaks usually blue shift and broaden as excitation increases. For the same reason, the GaAs peaks observed in Figure 4.1.2 was broader than the one peak observed in Figure 4.1.1. The main difference between the figures was the addition of an AlGaAs peak above 1.6 eV for wires with an AlGaAs shell, which was not visible in Figure 4.1.1. $Al_{0.33}Ga_{0.67}As$ was originally expected to give rise to a PL peak closer to 1.9 eV[34], but [35] has shown that MBE grown AlGaAs nanowires may have a lower Al content than thin films grown under the same conditions, and that AlGaAs nanowires grown under film conditions corresponding to 30% Al can display PL peaks around 1.60 eV to 1.65 eV.

As mentioned in section 2.8, it has previously been reported that GaAs nanowires with an AlGaAs shell have much higher QE than nanowires without an AlGaAs shell. This fact, in combination with the results discussed in this section, shows the importance of a passivation layer to measure nanowire PL as accurately as possible, as long as the shell PL does not overlap with that of the core.

5.2 Sample As539-3 PL power dependence

As mentioned in section 4.2, sample As539-3 consisted of AlGaAs nanowires with a GaAs insert. Because of the lower diffusion length of the Al atoms than the Ga atoms, the GaAs insert was covered with an AlGaAs shell. PL measurements were conducted on these nanowires in order to examine the PL emitted from WZ GaAs. The problem examining complete GaAs core nanowires is that completely stacking fault free nanowires are quite rare, and the GaAs PL observed may originate from type-II recombination at a short stacking fault, as shown in Figure 2.11.1, rather than purely in WZ. By studying GaAs insert instead, stacking fault free WZ GaAs PL should be much more frequently observed.

Interestingly, nine of the ten measured nanowires showed sharp PL peaks between 1.511 eV and 1.530 eV. This is still quite low compared to the free exciton previously observed from WZ GaAs nanowires at 1.544 eV[36]. The fact that the peaks observed in these measurements were 24 to 33 meV lower than the free exciton energy gives reason to believe they are related to carbon impurity in the GaAs insert, as the carbon neutral acceptor bound exciton should give rise to PL emission 26 meV lower than the free exciton[17].

NW09 stood out from the rest of the nanowires in sample As539-3 by displaying not a sharp peak at 1.52 eV, but a peak blue shifting from 1.482 eV to 1.509 eV. This may be a good indication of a stacking fault of a length of approximately 1.6 nm (see Figure 2.11.1), or a region with a high density of short stacking faults in the GaAs insert, and the corresponding type-II recombination.

The peak related to PL from AlGaAs was at higher energy for the nanowires of sample As539-3 than for the other GaAs/AlGaAs core/shell nanowires measured in this thesis, 1.633 eV to 1.668 eV compared to 1.611 eV. This shell PL peak at 1.611 eV corresponds well with reports of $Al_xGa_{1-x}As$ nanowires grown in MBE with the same conditions as thin film $Al_xGa_{1-x}As$ calibrated for x = 0.33[35], and indicates that the AlGaAs shell used as passivation layer for GaAs nanowires has an Al content of approximately 13%. From AlGaAs/AlGaAs core/shell nanowires such as sample As539-3, a type of self ordering mechanism has been observed between the core and the shell that results in a shell with higher Al content than the core. Furthermore, a gradient of the Al content along the length of the wire has been observed in the core, resulting in the lowest Al content in the

tip of the nanowire. This could explain why there are two different peaks observed in the PL spectrum of the nanowires of sample As539-3. The peaks at 1.67 eV could originate from the AlGaAs shell that has an increased Al content, while the sharp peak at 1.562 could originate from the low Al composition tip. The fact that there would be a limited region of the nanowire that contains the very lowest of Al composition, could also explain why a type of many-body effect could lead to band renormalization and subsequent red shift of the sharp PL peak.

If a linear change in the electronic band structure is assumed as the Al composition of $Al_xGa_{1-x}As$ increases from 0 to 0.33, the low Al composition tip peak at 1.562 eV corresponds to an Al content of approximately 6%, while the remaining believed shell peaks from 1.63 eV to 1.67 eV indicates an Al composition of 15% to 23%.

5.3 Effects of STEM and TEM on nanowire PL

As seen in Figure 4.3.2, Figure 4.3.3 and Figure 4.3.4, nanowire PL is impossible to measure after TEM imaging with a 200 kV acceleration voltage. Figure 4.3.5 and Figure 4.3.6 showed no significant change in PL after not being hit by the electron beam, but still being present in the TEM while imaging, further indicating that the electron beam is the source that induced non-radiative defects in the damaged nanowires, effectively destroying nanowire PL.

The figures in section 4.3 did, however, not show any particular change in PL from before and after STEM, and there was not found any correlation between acceleration voltage and specific change in nanowire PL. Also the nanowires in LPN2-4 not irradiated by the electron beam in STEM showed the same PL intensity change in the same amount as the irradiated nanowires. An interesting trend was, however, that the GaAsSb insert peak around 1.37 eV showed a lower excitation level after STEM. This trend was accompanied by a stronger AlGaAs peak at 1.6 eV. As can be seen from Appendix A, 62.5% of both the nanowires imaged and not imaged in STEM had an increase in AlGaAs peak strength. For the GaAs peak, only 13.3% and 25% of the nanowires imaged and not imaged showed an increase in peak strength, while the corresponding statistics for the GaAsSb peaks were 17.6% and 0%. Of course, this may be purely coincidental, but it may also indicate that the lifetime of excitons in the semiconductor nanowire was somehow reduced. If this was the case, the reduction in lifetime gives a reduction in diffusion length, and the probability of recombination at higher energy levels increases as recombination can take place before carriers are able to diffuse

to lower energy levels. Therefore, this would also explain the trend in reduced excitation level of the insert emission peaks. There was no particular difference in this trend for imaged and not imaged nanowires, so the reason for reduced lifetime could not be an effect of the electron beam. The reduction in lifetime might just be a sign of the nanowire degrading in contact with air as time goes by.

It would be hard to conclude from these results that a 30 kV electron voltage is below a threshold acceleration voltage that does not damage the nanowire PL by comparing with the 200 kV TEM imaging directly. Imaging by TEM gives a far greater dose of electrons than by STEM, and when taking into account that the TEM images of the nanowires studied in this thesis took roughly 30 times longer time to collect than the STEM images, comparing the electron dosage between STEM and TEM seems propostourus. What can be stated is that TEM imaging by a 200 kV acceleration voltage is damaging to nanowire PL. The number of non-radiative defects induced in the nanowire is most likely proportional to the number of electrons hitting the nanowire, and in that sense somewhat proportional to the amount of time the nanowire is subjected to the electron beam. It can also be said that it is quite safe to image the nanowires by STEM with a 30 kV acceleration voltage without damaging the nanowire, even for extended and thorough examination. It is, however, not safe to conclude that TEM with a 30 kV acceleration voltage would not cause damage. For this conclusion to be drawn, further measurements are needed.

5.4 Optically and structurally correlated examination of LPN2-4

Figure 4.4.1 showed the power dependent μ-PL measurements of NW2302, and the severely blue shifting peak from 1.32 eV to 1.4 eV. The blue shifting of the peak seemed to be a factor of both discrete peaks within the main peak with higher energy peaks growing stronger than lower energy levels as well as blue shifting of the discrete peaks. The blue shifting of the discrete peaks indicated that the recombination originates from a type-II hetero-junction, since the separation of electrons and electron holes causes a strong electric field to bend the electronic band structure continuously as the number of electron and electron holes increases in the two regions. In this case, it was thought that electrons would be confined mainly in a stacking fault of ZB GaAs near the insert, and electron holes would be confined in the GaAsSb insert as these regions represent the lowest energy level in the conduction band and the highest energy level in the valence band respectively. Also, the discrete peaks within the main peak shifting from lower energy peaks to higher energy peaks appear to be caused by band filling. For band filling to be as significant as seen in Figure 4.4.1, there would

have to be quantum confinement of the excitons. As explained in section 2.5, quantum confinement of excitons was not expected for inserts of 30 nm to 50 nm. This band filling would therefore also suggest that electrons are confined in a ZB region close to the insert, and that the region is so short that the electron energy level is quantized into discrete energy levels within the region. The broadness of the discrete peaks further suggest that the origin of the discrete peaks were not recombination in a type-I structure, but rather from spatially indirect transitions. However, slight variation of Sb composition along the insert might also explain a broadening of insert emission peaks.

As seen in Figure 4.4.2, there were stacking faults of ZB GaAs close to the insert in NW2302. One stacking fault a couple of nanometers from the insert, and one approximately 10 nm from the insert. However, both stacking faults seem a bit too short for there to be more than one energy level for electrons, even taking into consideration that the energy levels in section 2.11 were calculated assuming no overlapping of electron wave function with insert or other stacking faults. NW1102 would further suggest that the origin of the quantized electron energy levels are not the stacking faults. This is because Figure 4.4.3 showed the same type of blue shift as NW2302, but Figure 4.4.4 showed that the closest stacking fault to the insert was approximately 80 nm from the insert. Because the typical wavelength of an electron in a quantized energy level in a stacking fault is roughly 50 nm, there would be no overlapping of the wave function of an electron in this stacking fault and the electron holes in the insert, and spatially indirect recombination should be impossible. Taking this into consideration along with the fact that the typical energy difference between two discrete peaks are 5-20 meV, the insert emission could be explained by a region of ZB GaAs directly above the insert with an estimated length of 4-10 nm. Sadly, the TEM images only show contrast between different crystal structures, so there is no way of proving or disproving the presence of a ZB region of GaAs directly following the ZB GaAsSb region by TEM alone as this would only be displayed as WZ region followed by a ZB region and a new WZ region. If the nanowire growth directly after growth interrupt still favoured ZB, or there was a certain critical energy corresponding to phase change from ZB to WZ that was not reached until a few seconds after growth was resumed, the resulting ZB GaAs region would have to be measured by accurate and localized composition analysis along the nanowire.

As shown in Figure 4.4.5, NW1302 showed the same blue shift procedure as the two previous nanowires, despite the fact that this wire had both a twin defect in the insert slightly skew along the

nanowire axis and a region of 4H GaAs after the insert. This suggested that the twin defect does not significantly alter the electronic band structure in the insert, and further indicated that the stacking faults near the insert was the origin of quantized electron energy states.

As shown in Figure 4.4.7, the μ-PL measurements conducted on NW2101 resulted in a slightly different insert peak behavior than the previous nanowires, that being no observable separation of discrete energy peaks within the main peak. The insert peak was slightly asymmetric, with a broader lower energy side than higher energy side, suggesting that the discrete peaks were still present within the main peak although not clearly separable. As seen in Figure 4.4.8, the only visible structural difference between this wire and the first two was the density of stacking faults close to the insert. This suggested that a high density of stacking faults near the insert may degrade the quality of the observed insert emission peak by adding additional emission peaks on top of the true insert peaks.

As mentioned in section 4.4, there were also a few nanowires that displayed much less blue shifting than the nanowires previously discussed in this section. NW1103, presented in Figure 4.4.9, showed a blue shift of just 15 meV. However, like the other nanowires of LPN2-4 that showed little blue shift, the maximum intensity was lower than other nanowires that showed more blue shift of insert emission. The reduction in peak intensity means fewer excited carriers, and subsequently less band bending and band filling. The fact that there is little blue shift alone therefore doesn't mean that there is no ZB GaAs region directly at the insert. Furthermore, the peak is quite broad, which could indicate the presence of structural defects as seen in NW2101. As Figure 4.4.10 shows, there are multiple twins along the side of the insert, a diameter increase along the insert, and approximately only 30 nm of ZB GaAs below the insert before the break-off point of the nanowire. Twins closely stacked together like this may induce changes in the electronic band structure of the insert, causing the same effect as possibly seen by peak broadening in NW2101. The break-off point of the nanowire would leave the GaAs core exposed to the air, and there should be significantly more surface states in this region. This would lead to a site of a significant amount of non-radiative recombination, and there might be less carriers diffusing into the insert. The non-radiative site may therefore be the reason for little blue shift, rather then a pure ZB GaAsSb insert without ZB GaAs.

NW1203 and NW2201 also showed little blue shift of peaks around 1.35 eV, but as shown in Figure

4.4.14, there was no insert in NW2201. There was, however, presence of 4H and ZB regions of GaAs with twin defects. As seen in Figure 4.4.11 and Figure 4.4.13, the intensity of the peaks from 1.35 eV to 1.4 eV was quite low. It was unclear what was the cause of the weak insert emission in NW1203, but one theory was that the high density of stacking faults of variable length would give rise to reduced carrier mobility, and subsequently fewer excitons diffusing to the insert. NW2201 should not give any emission peaks in the insert emission region, but it was hypothesized that 4H might give PL peaks in this region. However, the reason why these two nanowires were given the space in this thesis, was the sharp PL peak at 1.390 eV in NW1203 and at 1.420 eV in NW2201. These peaks were of particular interest because of the degree of sharpness in the peaks, and the absence of blue shift. It was first thought that 4H might be the origin of this peak when observed in NW2201, but there was no 4H in NW1203. Because of no blue shift, it was thought to be quite unlikely for long stacking faults to be the origin of these peaks. Even though the weak intensity could cause no blue shift, the other even weaker peaks displayed blue shift. Furthermore, the peak seemed too sharp to be caused by spatially indirect recombination at stacking fault interfaces. Further attempts to explain these peaks resulted in the hypothetical possibility of incorporation of Au atoms in the GaAs core. There are many possibilities of different ways to incorporate Au impurities in the GaAs crystal structure (although very unlikely with VLS by MBE), but if this was the cause of the sharp peaks, also peaks at 1.07 eV should be visible[37]. However, the 1.07 eV range was not measured for the LPN2-4 sample. It was also doubtful that Au impurities would cause such a narrow peak, but further attempts to explain these peaks have so far not produced any good results.

5.5 PL of WZ versus ZB GaAs

Section 4.5 showed the comparison of PL from GaAs nanowires with a GaAsSb insert and an AlGaAs shell where the GaAs structure was both WZ (sample As540-8) and ZB (sample As540-9). If the hypothesis presented in section 5.4 about the origin of the blue shifting insert peak was from recombination between a ZB region of GaAs and the GaAsSb insert, there should be little difference in the photon energy of the insert PL peak at low laser excitation. However, as seen in Figure 4.5.1 and Figure 4.5.2, the photon energy difference in emerging insert emission peak appeared to be equal to the entire conduction band offset from ZB GaAs to WZ GaAs of 117 meV. This would suggest that both WZ and ZB GaAs nanowires produce a type-II DH when ZB GaAsSb regions are grown with this composition of Sb. This would also explain why the amount of blue shift observed in sample LPN2-4 sometimes was in the region of 115 meV (see Figure 4.4.1), which

is a bit too high to be explained by quantum confinement of electrons in a ZB region of GaAs alone.

But if there is no quantum confinement of electrons in a ZB region of GaAs, where does the observed band filling effect originate? An insert with a length of 30 nm to 50 nm in GaAs would not quantize the energy levels of excitons, as stated in section 2.5. However, if the structure is a type-II DH, where electrons and electron holes are not localized in the same regions, the main source of emission may not be exciton annihilation but rather free electrons at one side of the interface recombining with free electron holes on the other side. Also as explained in section 2.5, the energy levels of free carriers can be quantized at greater spatial dimensions than the exciton because their de Broglie wavelength is greater than the Bohr radius of the exciton. If the peaks observed at 1.21 eV in the nanowires of sample As540-9 corresponds to free electrons recombining with the lowest quantized energy levels of electron holes in the insert, and the sharp peak observed at 1.422 eV corresponds to an exciton formed by a defect bound electron in the insert combined with an electron hole, this would indicate that the valence band and conduction band offsets between ZB GaAs and ZB GaAsSb is approximately 300 meV and 216 meV, respectively.

By viewing the electron holes as confined within a quantum dot with a diameter of 50 nm with potential barriers of 216 meV, approximate values for the electron hole energy levels in a ZB GaAsSb insert in WZ GaAs can be calculated. The approximation of the light electron holes to be confined in a quantum dot with 216 meV barriers is actually a bit rough. The actual situation would rather be a quantum cube, which would give slightly lower values for the quantized energy levels. However, only the barrier induced by the interface between WZ GaAs and ZB GaAsSb would yield a 216 meV barrier. The barrier induced at the ZB GaAsSb – ZB AlGaAs interface would be much greater. Furthermore, the calculations are made considering the effective mass of electron holes in GaAs. The light electron effective mass in GaAsSb would be greater. The greater barrier would yield slightly higher values for the quantized energy levels of light electron holes, while the increased effective mass would yield lower quantized energy values. As these factors work against each other, the approximation of the quantum dot is expected to give a good indication of the actual quantized energy levels of light holes in the insert. These values were calculated for the light electron holes because the heavy holes have a greater momentum, and therefore shorter wavelengths and are not quantized in the same degree. The values are presented in Table 5.5.1.

Level	Energy [meV]
0	1.73
1	6.93
2	15.6
3	27.7
4	43.2

Table 5.5.1. Energy levels of light electron holes of GaAs in a 50 nm quantum dot with 216 meV barriers.

As seen in Table 5.5.1, the difference in photon energy between the different energy levels of light electron holes correspond well to the observed discrete peak difference observed in section 4.4 of 5-15 meV. The quantum confinement of light electron holes in a ZB GaAsSb insert of 50 nm in a GaAs nanowire with a 50 nm diameter is a likely explanation for the band filling effect observed in section 4.4. The type-II DH can also give an explanation for the two insert peaks observed from the same insert at different energies in Figure 4.5.1 and 4.5.2. If the Sb composition at the two heterojunctions of the insert is not the same, which is quite likely, this could lead to two distinct main PL peaks.

From the results discussed in this section, an approximation of what the band structure might look like is presented in Figure 5.5.1. The figure shows a different band structure than that which was expected from section 2.9, the main difference being the greater offset in conduction band. For an all ZB nanowire, this creates a strong type-II DH compared to the relatively weak that was expected[23]. It is possible that strain caused by the lattice mismatch of GaAs and GaAsSb changes the electronic band structure to what is depicted in Figure 5.5.1.
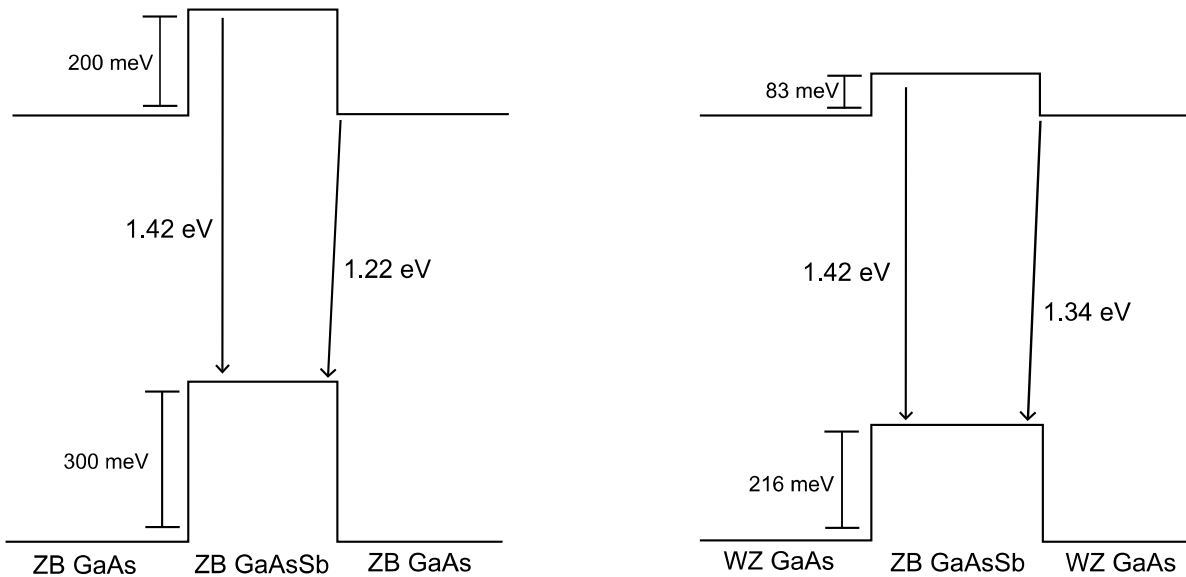
Figure 5.5.1. Approximation of possible electronic band structure in ZB nanowire and subsequent WZ nanowire electronic band structure.

Figure 5.5.2 shows what is believed to be the electronic band structure of the nanowires presented in section 4.4, and previously discussed in section 5.4. Though a ZB region of GaAs at the insert was believed to be the most probable origin of the observed band filling effect and band bending observed in section 4.4, the measurements presented in section 4.5 and discussed in this section strongly indicated this that there was no ZB region of GaAs at the insert. It was, however, showed that the quantization of three dimensionally confined electron holes in the insert presented in Table 5.5.1 and the band bending depicted by an approximated computer simulation in Figure 5.5.2 presented a viable explanation for the PL spectrum observed in section 4.4 and 4.5.

(a)   (b)
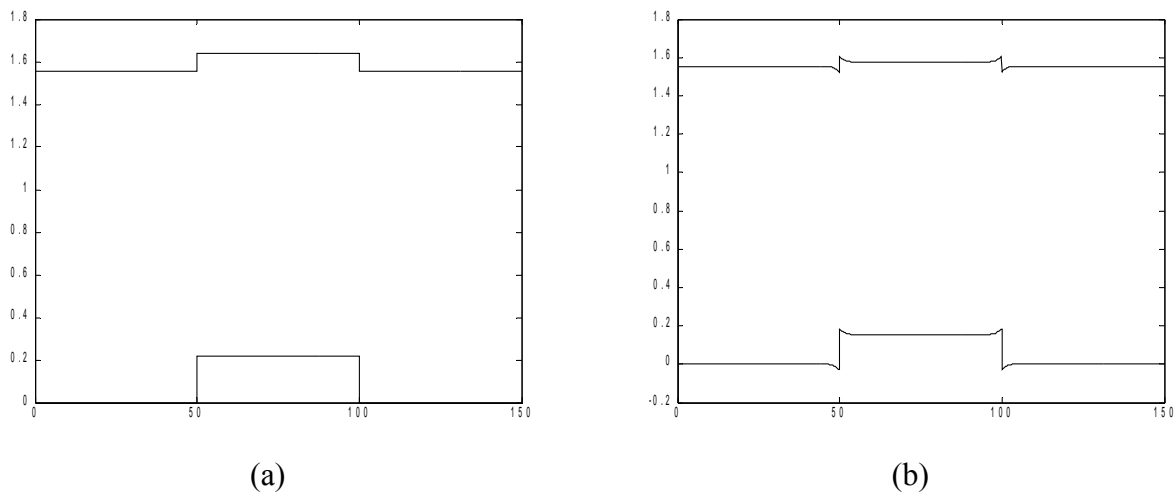
Figure 5.5.2. Approximated electronic band structure [eV] as a function of position [nm] in a WZ GaAs nanowire with a ZB GaAsSb insert and (a) no band bending (b) severe band bending.

62

5.6 Polarization of nanowire PL

Figure 4.6.1 showed the polarization dependence of PL from sample As539-3, which was all WZ AlGaAs nanowires with a GaAs insert. Most peaks in NW07 and NW08 showed exemplary behavior for what was expected of PL peaks originating from exciton annihilation in the WZ structure, that being mostly polarized in the direction perpendicular to the nanowire axis. The peaks observed in NW09 and NW10 were not polarized strongly in the perpendicular direction, but the fact that they were not polarized in the parallel direction still indicates WZ originated PL as this suggests image effect is not the only physical effect controlling the polarization properties of the nanowires.

Figure 4.6.2 showed the polarization dependence of NW1303 and NW3103 of sample LPN2-4, which was WZ GaAs nanowires with a ZB GaAsSb insert and an AlGaAs shell. The figure shows a strong parallel polarization of the insert originated peak, and perpendicular polarization of the GaAs and AlGaAs originated peaks. This corresponds well with the fact that the inserts were ZB, and should have a parallel polarization, while the WZ GaAs and AlGaAs would give perpendicular. Figure 4.6.3 showed the polarization dependence of the same type of wires, but from sample As540-8. The peaks in this figure showed the same trend of parallel polarization of insert emission, and slight perpendicular polarization of GaAs and AlGaAs peaks.

Figure 4.6.3 showed the polarization dependence of NW03, NW05 and NW06 of sample As540-9, which was ZB GaAs nanowires with a ZB GaAsSb insert and an AlGaAs shell. Although PL from an all ZB nanowire would be expected to be polarized parallel to the nanowire axis, the GaAs and AlGaAs peaks in NW03 and NW05 displayed slight perpendicular polarization. This would suggest that there are stacking faults of WZ in the ZB nanowires, and that the PL peaks of GaAs and AlGaAs mainly originate from spatially indirect recombination of electron holes confined in the WZ stacking faults and electrons in the ZB regions nearby. Because the electron holes are confined in the WZ crystal structure, the selection rules dictate that the resulting recombination emission is perpendicularly polarized. The GaAs peak in NW06 displayed parallel polarization, but not quite as strong as expected for pure ZB. This may give an indication that NW06 suffered from less stacking faults than the two other nanowires.

6. Conclusion

GaAs nanowires with both a WZ and ZB crystal structure with ZB GaAsSb inserts and both with and without an AlGaAs shell were subjected to μ-PL measurements at low temperature. Through interpretation of μ-PL measurements, the significance of the AlGaAs passivation layer was presented. Selected nanowires with the WZ GaAs structure were subjected to μ-PL, STEM and TEM, and attempts to correlate the specific structure of the different nanowires with their optical properties were presented. It was also shown that STEM at 30 kV did not significantly change the optical properties of the nanowire, but TEM imaging at 200 kV was discovered to completely destroy the observable PL of nanowires.

Also nanowires consisting of GaAs inserts in AlGaAs nanowires were measured in μ-PL spectroscopy, and it was found that the free exciton was rarely observable as peaks mostly showed carbon impurity related emission. Through comparison of WZ and ZB GaAs nanowires, the electronic band structure of the GaAsSb insert was found to, very likely, be a type-II DH for both types of nanowires. Also, an explanation for the physical origin of the insert emission behavior was presented. Through interpretation of polarization dependent μ-PL measurements, the theoretical polarization properties of nanowire PL was observed to coincide well with observations, but also indicated a strong presence of WZ stacking faults in the ZB GaAs nanowires measured in this thesis.

7. Literature Cited

[1]   C. Kittel and P. McEuen, *Introduction to solid state physics*. Hoboken, N.J.: Wiley, 2005.

[2]   A. Greytak*, et al.*, "Semiconductor nanowire laser and nanowire waveguide electro-optic modulators," *Applied physics letters,* vol. 87, p. 151103, 2005.

[3]   L. Chen and E. Towe, "Nanowire lasers with distributed-Bragg-reflector mirrors," *Applied physics letters,* vol. 89, p. 053125, 2006.

[4]   M. Stevens*, et al.*, "Infrared wavelength-dependent optical characterization of NbN nanowire superconducting single-photon detectors," *Journal of modern optics,* vol. 56, pp. 358-363, 2009.

[5]   ITRS. 28.10.2009, *International Technology Roadmap for Semiconductors 2007 report*. Available: http://www.itrs.net/Links/2007ITRS/ExecSum2007.pdf

[6]   R. Ma*, et al.*, "Light Coupling and Modulation in Coupled Nanowire Ring-Fabry-Perot Cavity," *Nano letters,* vol. 9, pp. 2697-2703, 2009.

[7]   R. Yan*, et al.*, "Nanowire photonics," *Nature Photonics,* vol. 3, pp. 569-576, 2009.

[8]   S. Lee*, et al.*, "P-type Si-nanowire-based Field-effect Transistors for Electric Detection of a Biomarker: Matrix Metalloproteinase-9," *THE JOURNAL OF THE KOREAN PHYSICAL SOCIETY,* vol. 55, pp. 232-235, 2009.

[9]   M. Borgstrom*, et al.*, "Optically bright quantum dots in single nanowires," *Nano letters,* vol. 5, pp. 1439-1443, 2005.

[10]   C. Barrelet*, et al.*, "Hybrid single-nanowire photonic crystal and microresonator structures," *Nano letters,* vol. 6, pp. 11-15, 2006.

[11]   D. Spirkoska*, et al.*, "Structural and optical properties of high quality zinc-blende/wurtzite GaAs nanowire heterostructures," *Physical review. B, Condensed matter and materials physics,* vol. 80, p. 245325, 2009.

[12]   F. Glas*, et al.*, "Why Does Wurtzite Form in Nanowires of III-V Zinc Blende Semiconductors?," *Physical Review Letters,* vol. 99, p. 146101, 2007.

[13]   B. G. Streetman and S. Banerjee, *Solid state electronic devices*. Upper Saddle River, N.J.: Pearson/Prentice-Hall, 2006.

[14]   Ioffe. 03.05.2010, *GaAs material properties*. Available:
        http://www.ioffe.ru/SVA/NSM/Semicond/GaAs/bandstr.html

[15]   M. C. Gupta, *Handbook of photonics*, 1st ed. Boca Raton, Fla.: CRC Press, 1997.

[16]   Ioffe. 03.05.2010, *GaAs(1-x)Sb(x) material properties*. Available:
        http://www.ioffe.ru/SVA/NSM/Semicond/GaAsSb/bandstr.html

[17]   G. Gilliland, "Photoluminescence spectroscopy of crystalline semiconductors," *Materials science & engineering. R, Reports,* vol. 18, pp. 99-399, 1997.

[18]   B. E. A. Saleh and M. C. Teich, *Fundamentals of photonics*, 2nd ed. Hoboken, N.J.: John Wiley & Sons, Inc., 2007.

[19]   S. Birner. 03.05.2010, *Next generation 3D nanodevice simulator*. Available:
        http://www.nextnano.de/nextnano3/tutorial/1Dtutorial_QW_exciton.htm

[20]   R. Wagner and W. Ellis, "VAPOR-LIQUID-SOLID MECHANISM OF SINGLE CRYSTAL GROWTH (NEW METHOD GROWTH CATALYSIS FROM IMPURITY WHISKER EPITAXIAL + LARGE CRYSTALS SI E)," *Applied physics letters,* vol. 4, p. 89, 1964.

[21]   M. Tchernycheva*, et al.*, "Temperature conditions for GaAs nanowire formation by Au-assisted molecular beam epitaxy," *Nanotechnology,* vol. 17, pp. 4025-4030, 2006.

[22]   H. L. Zhou*, et al.*, "Wurtzite GaAs/AlGaAs core-shell nanowires grown by molecular beam epitaxy," *Nanotechnology,* vol. 20, p. 415701, 2009.

[23]   T. Wang*, et al.*, "Characterization of band gap in GaAsSb/GaAs heterojunction and band alignment in GaAsSb/GaAs multiple quantum wells," *Materials science & engineering. B, Solid-state materials for advanced technology,* vol. 147, pp. 131-135, 2008.

[24]   M. Murayama and T. Nakayama, "CHEMICAL TREND OF BAND OFFSETS AT WURTZITE ZINCBLENDE HETEROCRYSTALLINE SEMICONDUCTOR INTERFACES," *Physical review. B, Condensed matter,* vol. 49, pp. 4710-4724, 1994.

[25]   H. Ruda and A. Shik, "Polarization-sensitive optical phenomena in semiconducting and metallic nanowires," *Physical review. B, Condensed matter and materials physics,* vol. 72, p. 115308, 2005.

[26]   G. Samara, "TEMPERATURE AND PRESSURE DEPENDENCES OF THE DIELECTRIC-CONSTANTS OF SEMICONDUCTORS," *Physical review. B, Condensed matter,* vol. 27, pp. 3494-3505, 1983.

[27]   Ioffe. 09.05.2010, *Basic Al(x)Ga(1-x)As Parameters*. Available: http://www.ioffe.ru/SVA/NSM/Semicond/AlGaAs/basic.html

[28]   P. Mohseni and R. LaPierre, "A growth interruption technique for stacking fault-free nanowire superlattices," *Nanotechnology,* vol. 20, p. 025610, 2009.

[29]   J. Bauer*, et al.*, "VLS growth of GaAs/(InGa)As/GaAs axial double-heterostructure nanowires by MOVPE," *Journal of Crystal Growth,* vol. 310, pp. 5106-5110, 2008.

[30]   R. Waser, *Nanoelectronics and information technology: advanced electronic materials and novel devices*, 2nd ed. Weinheim: Wiley-VCH, 2005.

[31]   Newport. 06.05.2010, *Millennia Pro Series Specifications*. Available: http://www.newport.com/Millennia-Prime-532-nm-CW-DPSS-Lasers/501529/1033/catalog.aspx?Section=Spec

[32]   Andor. 06.05.2010, *Newton EMCCD Specifications*. Available: http://www.andor.com/scientific_cameras/newton/models/default.aspx?iProductCodeID=48

[33]   Janis. 06.05.2010, *ST-500 Microscopy Cryostat Specifications*. Available: http://www.janis.com/products/productsoverview/SuperTranContinuousFlowCryostatSystems/ST-500MicroscopyCryostat.aspx#

[34]   K. Zhuravlev*, et al.*, "Photoluminescence of high-quality AlGaAs layers grown by molecular-beam epitaxy," *Applied physics letters,* vol. 76, pp. 1131-1133, 2000.

[35]   Z. Wu*, et al.*, "Growth and photoluminescence characteristics of AlGaAs nanowires," *Applied physics letters,* vol. 85, pp. 657-659, 2004.

[36]   T. Hoang*, et al.*, "Observation of free exciton photoluminescence emission from single wurtzite GaAs nanowires," *Applied physics letters,* vol. 94, p. 133105, 2009.

[37]   A. Gutkin*, et al.*, "PHOTOLUMINESCENCE ASSOCIATED WITH AUGA CENTERS IN GAAS-AU," *Soviet physics. Semiconductors,* vol. 25, pp. 307-309, 1991.

8. Appendix A

LPN 2-4 pre and post STEM

Nanowire	Acceleration voltage	Relative dosage	Laser intensity	AlGaAs peak ΔĨ	AlGaAs ΔE_cph	AlGaAs ΔFWHM	GaAs peak ΔĨ	GaAs ΔE_cph	GaAs ΔFWHM	GaAsSb peak ΔĨ	GaAsSb ΔE_cph	GaAsSb ΔFWHM	Note
NW1101	5 kV	1X	40 µW	2006,10%	-2,27	-59,74%	1038,68%	2,74	27,30%	-31,53%	-12,42	0,13%	GaAs and AlGaAs nearly not visible pre-STEM
NW1102	5 kV	1X	500 nW	-86,56%	-10,49	-101,50%	-76,47%	8,39	27,00%	-35,64%	-4,50	-6,49%	AlGaAs peak has several higher energy peaks
NW1103	5 kV	5X	15 µW	-30,93%	-2,73	-20,50%	-37,80%	2,97	32,79%	-29,24%	0,19	-8,67%	GaAs peak not visible before high excitation
NW1201	10 kV	1X	5 µW	25,97%	-0,93	-4,19%	------	------	------	-39,23%	-4,71	-39,99%	
NW1202	10 kV	1X	10 µW	23,86%	-2,44	-19,72%	105,74%	-1,53	16,27%	-11,99%	-8,04	-23,40%	Also small peak at 1,3 eV
NW1204	10 kV	5X	10 µW	20,58%	-2,23	-2,58%	-82,15%	-12,31	-101,59%	------	------	------	No GaAsSb peak, AlGaAs peak is a doublepeak
NW1301	15 kV	1X	20 µW	-81,72%	-0,57	30,52%	------	------	------	-12,43%	0,14	2,01%	No GaAs peak
NW1302	15 kV	1X	5 µW	43,88%	0,57	2,40%	-36,31%	1,19	-100,31%	-54,31%	-6,90	-32,77%	
NW1303	15 kV	5X	5 µW	-55,30%	6,06	-32,39%	-16,22%	6,12	-2,10%	112,68%	10,25	-11,75%	Two GaAs peaks
NW2101	30 kV	1X	1 µW	------	------	------	-7,77%	4,14	-14,54%	-62,27%	-3,66	-5,08%	No AlGaAs peak
NW2103	30 kV	5X	5 µW	-1,89%	1,99	-0,82%	-14,50%	-0,01	-4,77%	-60,58%	-5,07	45,86%	Several GaAs peaks, GaAsSb peaks measured at 10 µW
NW2104	30 kV	1X	10 µW	-50,86%	0,84	31,70%	-43,56%	------	124,47%	-22,29%	0,91	-21,44%	Change in GaAs and GaAsSb photon energy looks like band filling effect
NW2201	25 kV	1X	30 µW	9,89%	-0,78	9,76%	-31,45%	-3,10	-24,01%	126,29%	2,55	-27,96%	Several GaAs and GaAsSb peaks
NW2202	25 kV	1X	500 nW	------	------	------	------	------	------	-53,75%	2,55	8,22%	Almost no AlGaAs and GaAs PL
NW2203	25 kV	5X	5 µW	14,25%	0,39	-11,92%	-15,50%	-1,52	-28,37%	82,41%	0,52	5,10%	
NW2301	20 kV	1X	1 µW	46,83%	0,98	9,27%	-22,55%	2,56	------	-60,52%	-1,74	-14,69%	GaAs peaks measured at 20 µW, too broad for FWHM
NW2302	20 kV	1X	1 µW	231,37%	3,40	-1,02%	-100,00%	------	------	-70,23%	-11,35	-53,58%	AlGaAs peak much bigger, GaAs peak almost disappeared like NW2103
NW2303	20 kV	5X	500 nW	95,11%	-0,19	-15,99%	-16,82%	-2,20	30,03%	-36,06%	-6,80	2,64%	Two GaAs peaks
NW3101	0 kV	0X	5 µW	61,16%	0,57	-4,75%	-4,92%	0,85	-1,87%	-16,07%	0,54	-9,46%	
NW3102	0 kV	0X	5 µW	-44,68%	3,81	-27,98%	------	------	------	-55,53%	-2,89	-54,74%	GaAs peak not visible post-STEM, GaAsSb measured at 1 µW
NW3103	0 kV	0X	500 nW	------	------	------	0,19%	0,67	-19,39%	-37,85%	1,20	4,85%	Very low AlGaAs peak
NW3201	0 kV	0X	1 µW	14,74%	0,00	-4,81%	-2,14%	2,36	-24,08%	-34,26%	-1,84	-29,03%	GaAs and AlGaAs peaks looks almost identical pre and post STEM
NW3202	0 kV	0X	40 µW	43,59%	8,92	0,20%	-38,46%	1,02	10,68%	------	------	------	Looks like two or more wires excited differently, so compared at very high excitation for more uniform comparison. GaAsSb peaks too complex for simple comparison.
NW3203	0 kV	0X	500 nW	77,36%	2,29	-14,85%	-15,94%	1,85	11,41%	-59,70%	-9,51	-24,49%	
NW3301	0 kV	0X	5 µW	-60,54%	1,52	13,12%	-32,23%	2,55	41,14%	-19,00%	0,00	-6,40%	
NW3302	0 kV	0X	500 nW	41,86%	-3,28	-20,88%	13,64%	3,64	------	-43,16%	0,69	-15,46%	Two GaAs peaks, GaAs FWHM inaccurate since peak distribution seems to be at different stages for pre and post STEM.
NW3303	0 kV	0X	10 µW	-23,25%	-1,51	-3,76%	-65,71%	4,26	23,09%	-43,31%	-5,56	7,47%	